# LEARNING LOW RANK NEURAL REPRESENTATIONS OF HYPERBOLIC WAVE DYNAMICS FROM DATA

WOOJIN CHO, KOOKJIN LEE, NOSEONG PARK, DONSUB RIM AND GERRIT WELPER

ABSTRACT. We present a data-driven dimensionality reduction method that is well-suited for physics-based data representing hyperbolic wave propagation. The method utilizes a specialized neural network architecture called low rank neural representation (LRNR) inside a hypernetwork framework. The architecture is motivated by theoretical results that rigorously prove the existence of efficient representations for this wave class. We illustrate through archetypal examples that such an efficient low-dimensional representation of propagating waves can be learned directly from data through a combination of deep learning techniques. We observe that a low rank tensor representation arises naturally in the trained LRNRs, and that this reveals a new decomposition of wave propagation where each decomposed mode corresponds to interpretable physical features. Furthermore, we demonstrate that the LRNR architecture enables efficient inference via a compression scheme, which is a potentially important feature when deploying LRNRs in demanding performance regimes.

#### 1. Introduction

Hyperbolic waves arise in models of inviscid fluids such as gases or depth-integrated surface flows like tsunamis [71, 108, 99, 67, 31, 69]. These waves are characterized by long-range propagation, shock formation, and nonlinear interactions, all occurring without dissipation or dispersion. The defining attributes of these waves are the placement of sharp features along smooth curves and the continuous evolution of these curves with respect to time and geometry [104]. More generally, similar patterns are encountered in systems that do not explicitly model hyperbolic waves. The smooth placement of edges and curves is widely observed in data across a range of scientific and engineering domains [80, 76, 63, 61]. The routine manifestation of wave-like structure in data underscores the fundamental importance of computational methods that can learn efficient representations of such structures in a data-driven manner.

The main subject of this paper is an efficient representation of hyperbolic wave dynamics based on neural networks with a specialized architecture, one that is supported by theory and can be learned directly from data alone through deep learning techniques. The representation is based on a new notion of low dimensionality and is built on an implicit neural representation family called the low-rank neural representation (LRNR) introduced in recent works [27, 96, 26]. We aim to establish that LRNRs exhibit several desirable properties in the data-driven setting. First, LRNRs are efficient representations in the sense that they provide a low-dimensional encoding of the data by mapping it to a low-dimensional latent or coefficient space in a stable manner. Second, they induce a new decomposition of wave phenomena into interpretable features. Third, the dynamics governing the latent variables are highly regular, that is, they vary smoothly in time; this key property, first observed in the theoretical construction [96], is also observed empirically in LRNRs trained from data as we shall demonstrate. Fourth, the LRNR architecture enables accelerated evaluation and backpropagation computations; this is challenging to achieve with generic architectures. These properties make LRNRs promising candidates for reduced or surrogate models for solving partial differential equations (PDEs), as proposed in [27, 26].

Date: October 30, 2025.

Traditionally, sparsity has been one prominent measure of efficiency for data representations, and there is a substantial body of literature devoted to finding sparse representations of wave propagation using dictionaries or frames such as wavelets, curvelets, and shearlets [109, 37, 76, 20, 61, 33]. These approaches are highly relevant to the study of digital images, which also display sharp features aligned along smooth curves, such as the edges of rigid objects in photographic images; these features are sometimes modeled by so-called cartoon-like functions, indicator functions over spatial regions with smooth boundaries [85, 14, 36, 77, 10]. Another class of important constructions arises from a slightly different motivation, in works from numerical analysis that seek to devise efficient representations compatible with numerical methods for solving PDEs, such as finite volume methods or discontinuous Galerkin methods [67, 51]. In adaptive mesh refinement (AMR) methods, the grid representation of a propagating wave is refined to have higher resolution locally near shock discontinuities [8, 7]. These two perspectives, the approximation-theoretic and the numerical-analytic, have also been studied in conjunction, for example in the development of various discretizations of Fourier integral operators [18, 19].

Low rank neural representation and compositional low-rankness. The LRNR is based on a different theoretical notion of efficiency, one that incorporates the compositional structure seen in deep learning models. To illustrate the basic idea, we consider a simple example involving the wave equation  $(\partial_{tt} - c^2 \partial_{xx})u = 0$  in one spatial dimension. The solution is given by the d'Alembert formula [41, 40]

(1.1) 
$$u(x,t) = f(x - ct) + g(x + ct),$$

for some one-dimensional functions f and g. Intuitively, one observes that four spatial functions are used in this construction: the pair  $f(\cdot)$  and  $g(\cdot)$  describing the wave profiles, along with the pair  $\mathrm{Id}(\cdot)$  and  $\mathrm{Id}(\cdot)$  (the identity map and the constant function, respectively) which comprise the expression for the translation

$$(1.2) x \pm ct = \operatorname{Id}(x) \pm ct \cdot 1(x),$$

where the scalars  $\pm ct$  play the role of time-dependent coefficient variables. Since the set of four functions  $\{f, g, \text{Id}, 1\}$  determines the solution to the wave equation, one may view the solution as a four-dimensional object. This perspective highlights a fundamental property of waves that is already familiar to the reader: their solutions can be written as a composition of a small number of interpretable components, some related to the shape of the wave profile and others related to the propagation of the wave.

The LRNR architecture was devised to exploit this notion of dimensionality, relying on a generalization referred to as a compositional low-rank structure. This structure is motivated by structures in nonlinear waves satisfying scalar conservation laws that are much more complicated than the d'Alembert solution [96]. The LRNR architecture is central to describing this structure, so we introduce it here informally and defer the technical definition of LRNRs until Sec. 2.1.

We begin with a feedforward neural network that maps spatial inputs to physical outputs, that is, an implicit neural representation (INR) [84, 101]. A LRNR is defined as a family of feedforward neural networks with depth L where each weight matrix  $\mathbf{W}^{\ell}$  and bias vector  $\mathbf{b}^{\ell}$  is expressed as a linear combination of rank-1 weights  $\mathbf{W}^{\ell}_{i}$  and biases  $\mathbf{b}^{\ell}_{i}$ . Suppose these rank-1 weights and biases are provided to us and are fixed; then  $\mathbf{W}^{\ell}$  and  $\mathbf{b}^{\ell}$  take linear combinations of the fixed matrices and vectors and only their coefficients are allowed to vary. If we denote these coefficients by a vector  $\mathbf{s} = (s^{\ell}_{p,i})_{p,i,\ell}$  whose entries are selected through indices  $p,i,\ell$  then we can write the weights and biases as, for example,

(1.3) 
$$\mathbf{W}^{\ell}(\mathbf{s}) = \sum_{i=1}^{r_1^{\ell}} s_{1,i}^{\ell} \mathbf{W}_i^{\ell}, \qquad \mathbf{b}^{\ell}(\mathbf{s}) = \sum_{i=1}^{r_2^{\ell}} s_{2,i}^{\ell} \mathbf{b}_i^{\ell}.$$

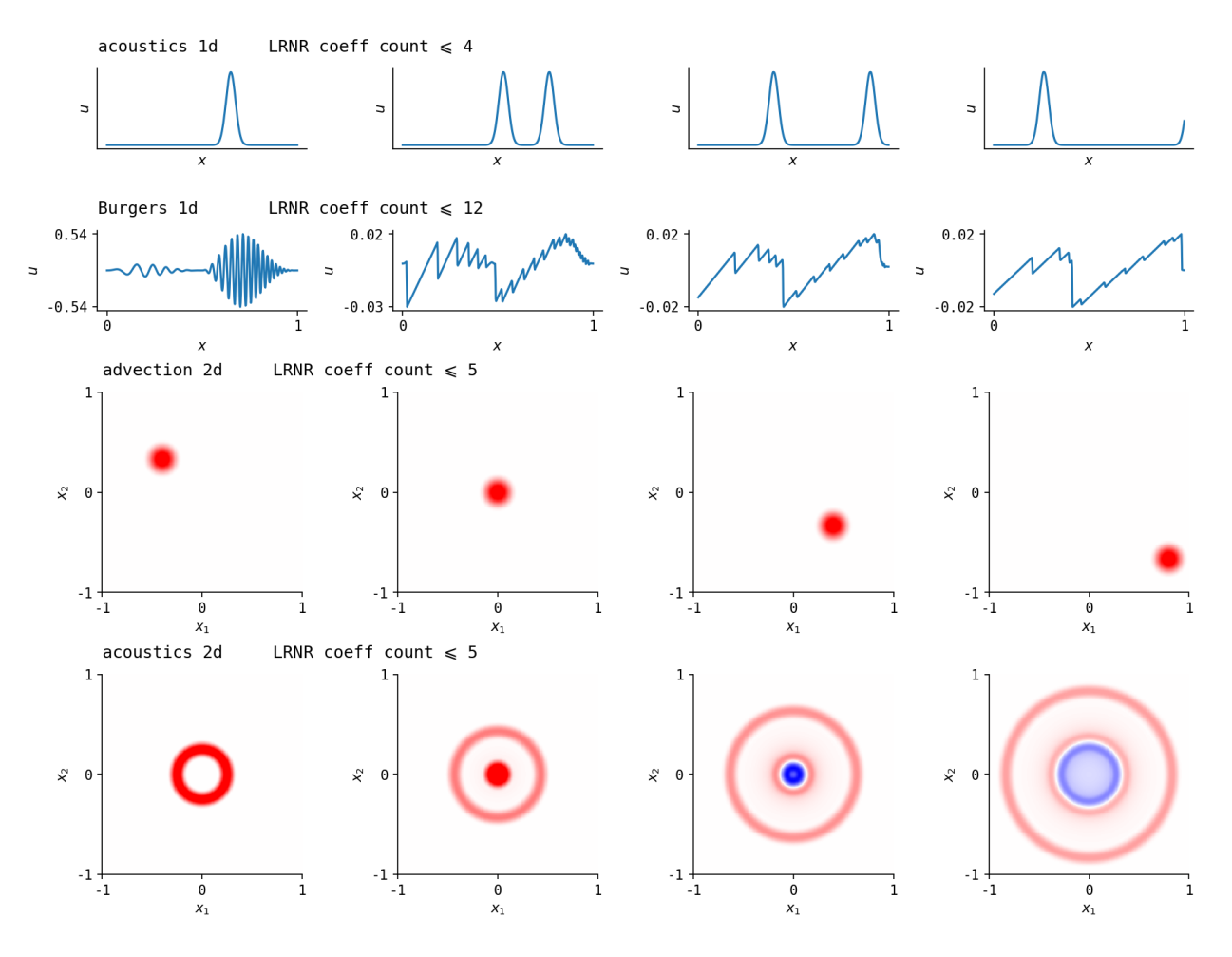


FIGURE 1. Various solution manifolds of time-dependent problems  $\mathcal{M} = \{u(\cdot,t) \mid t \in [0,T]\}$  and their LRNR coefficient counts  $\mathscr{C}$  (technical definition below in Def. 3.1). The solution of 1d and 2d wave equations, as well as the 1d and 2d advection equations, have a coefficient count of at most five (Thms. 3.2 and 3.3). Solution manifolds of scalar conservation laws (e.g., the 1d Burgers' equation) have a coefficient count of at most twelve (Thm. 3.4).

We denote the vector of layer-wise ranks  $\mathbf{r}=(r_p^\ell)_{p,\ell}\in\mathbb{R}^{2L}$ , where each entry represents the rank of a specific weight  $r_1^\ell$  or bias  $r_2^\ell$  at a certain layer  $\ell$ . The total number of coefficients in this case is given by the 1-norm of  $\mathbf{r}$ , that is,  $n=\|\mathbf{r}\|_1=\sum_{p,\ell}r_p^\ell$ . The width M of a LRNR is given by the largest matrix row dimension of the weight matrices  $\mathbf{W}^\ell$  over all layers.

We denote by  $\mathcal{H}_{\mathbf{r},M}$  the set of all LRNRs of rank  $\mathbf{r}$  and width M. Given a LRNR  $\mathcal{H}_{\mathbf{r},M}$ , its member  $h \in \mathcal{H}_{\mathbf{r},M}$  can be viewed as an INR  $h = h(\cdot; \mathbf{s})$  parametrized by its coefficients  $\mathbf{s} \in \mathbb{R}^n$ . This is a slightly more general version of LRNR introduced in previous works [27, 96, 26].

The LRNR coefficient count. We can make a connection between the total number of LRNR coefficients n discussed above and the notion of dimensionality discussed earlier in connection with the d'Alembert solution. To do so, we introduce an approximation theoretic notion in terms of the number of coefficients. Informally, given a collection of spatial functions  $\mathcal{M}$ , its LRNR coefficient count  $\mathscr{C}$  is defined as the minimal number of LRNR coefficients n required to construct a convergent approximation of the functions in  $\mathscr{M}$  with uniform approximation rate  $\alpha$  with respect to the width

M (precise definition in Sec. 3.1). In this work, we consider the collection  $\mathcal{M}$  made up of solutions to initial value problems in a given time window  $\mathcal{M} = \{u(\cdot,t) \mid t \in [0,T]\}.$ 

For solutions to representative hyperbolic problems, upper bounds can be established for their coefficient counts; see the gallery shown in Fig. 1. For example, the d'Alembert solution discussed above has a LRNR coefficient count of at most four, which matches the count of four functions noted earlier in (1.1-1.2). The entropy solution to the scalar conservation law  $\partial_t u + \partial_x F(u) = 0$  where the flux function is smooth and strictly convex (F'' > 0) is significantly more complex than the wave equation, and is characterized by nonlinear shock formation and interaction. Recent work [96] yields an upper bound on the coefficient count of an entropy solution: it is at most twelve.

For the wave equation in higher spatial dimensions, the analogue of the d'Alembert solution is the Lax-Phillips translational representation [65] based on the planar wave decomposition of the solution expressed in terms of the Radon transform. In this work, we show that the LRNR coefficient count of the solution to the d-dimensional wave equation is at most d+3 via a plane wave decomposition in the form of neural networks. This low dimensionality of the wave equation was previously discussed in [90, 91, 72], and the construction is a type of barycenter in the sliced Wasserstein metric [15, 30]. On the other hand, lower bounds or optimal constructions have not yet been established, and they appear particularly challenging to prove, especially for deeper networks with more than two layers (L > 2); new insights appear necessary for lower bounds.

Training LRNR from data. This work presents the first results on training LRNRs directly from data, particularly for data that consist of solutions to hyperbolic problems. The theoretical results confirm the existence of efficient LRNRs of hyperbolic waves, but they do not provide computational methods for training LRNRs directly from data. We aim to show that the training can be performed by standard gradient-based learning algorithms together with a combination of techniques including hypernetworks, learning rate scheduling, regularization, and adaptively weighted loss functions. We note that hypernetworks [48] have been widely used in conjunction with families of INRs to represent continuous fields representing a collection of physical objects. They serve as an alternative to directly learning latent variables as inputs [84], and they were used successfully in conjunction with well-established INRs like SIREN [101]. Our approach uses hypernetworks to represent the dependence of neural network parameters on physical parameters like time when such data are available. The Neural Implicit Flow (NIF) [83] is based on a similar physical-to-network parameter hypernetwork approach, although the precise form of dependence is similar to that of SIRENs, but distinct from our approach. Some operator learning approaches, such as DeepONet [73] or PCA-Net [49, 12], can be viewed as hypernetwork frameworks as well.

We report an important property of LRNRs trained on data, namely the regularity in the dynamics of the coefficients. This was an important property seen in the theoretical constructions. In the d'Alembert solution discussed above, the time-dependent coefficients  $\mathbf{s}(t)$  are linear  $t \mapsto \pm ct$  with respect to t (1.2) and hence have highly regular dependence; in the theoretical LRNR construction for entropy solutions [96], it was emphasized that the coefficients  $\mathbf{s}$  vary linearly with respect to time; in the theoretical construction for the wave equation in all dimensions below, the time-dependent coefficients are also linear in time. While these theoretical constructions do not necessarily imply that the LRNRs trained on data will have such properties, this work provides empirical evidence that LRNRs trained on data via gradient descent also display temporal regularity in the learned coefficient variables. Notably, this regularity is observed even when the wave data contain jump discontinuities.

The LRNR has another distinguishing property that can potentially be important for performance: The low-rank structure built into its architecture enables it to be compressed. The compressed versions are referred to as FastLRNRs and serve as accurate surrogates [26]. Here we demonstrate that LRNRs trained on wave data can be evaluated efficiently using this compression scheme, with the computational complexity scaling in terms of the rank  $\|\mathbf{r}\|_{\infty}$  rather than the width

M which can potentially be large. This property is useful in practice, as it allows LRNRs with large widths to approximate complex wave profiles, while simultaneously allowing LRNRs to be evaluated efficiently. To the best of our knowledge, this property has not been discussed for other proposed INRs (see discussions of performance in [79, 57]). A previous work by the authors [26] has applied this compression scheme to approximate backpropagation in physics-informed neural networks, leading to accelerated gradient descent iterations. From a deep learning perspective, this compression can be interpreted as a form of student-teacher knowledge transfer, or knowledge distillation [16, 53].

In this work we report the following training results. We train LRNRs on solution data from hyperbolic problems such as the compressible Euler equations, variable speed advection equation, Burgers' equation, and acoustic wave equations. We show that an adaptation of the meta-learning approach discussed in [27, 26] leads to an additional form of dimensionality reduction, appearing as low-rank tensors in the architecture; this falls beyond the existing modes of dimensionality reduction. We observe that this new reduction induces interpretable behavior when LRNRs are extrapolated along what we call *hypermodes*: it enables accurate and efficient tangent space representations and displays remarkably coherent extrapolation. We also demonstrate that FastLRNR compression [26] can be used to evaluate these models efficiently at fixed spatial points. Finally, we discuss the spatial extrapolation behavior of trained LRNR models, which exhibits wave propagation consistent with space-time causality in hyperbolic systems.

Other related works. There are relevant approximation theoretical results relating transport equations, reduced models, and neural networks. Results regarding parametric linear transport equations were proved for smooth convective fields in [64], where the initial condition and the smooth characteristic curves are approximated [114, 85]. Neural networks were shown to match the efficiency of reduced basis methods [44, 62]. The notion of compositional sparsity was introduced in [32]. These results mainly concern generic feedforward architectures. We mention another architecture inspired by solutions to Hamilton-Jacobi equations [34].

More broadly, the LRNR-based framework is closely related to model reduction in scientific computing, which aims to construct efficient representations of solutions to partial differential equations in order to accelerate computation. Classical approaches in this domain rely on linear approximations, such as a reduced basis approximation [50, 6], but their applicability is limited in many practical settings. This is especially true for hyperbolic wave problems, where sharp features propagate and interact in complex ways [97, 82, 107, 1, 92]. The challenge is referred to as the Kolmogorov barrier, reflecting the fundamental limitations of linear approximation as quantified by the Kolmogorov n-width [86]. Many articles proposed approaches that aim to overcome the Kolmogorov barrier: Template-fitting [97], method of freezing [11, 81], shock reconstruction [29], approximated Lax-Pairs [45], advection modes [55], transported snapshot interpolation (TSI) [107], shifted proper orthogonal decomposition (sPOD) [89], calibrated manifolds [17], Lagrangian basis method [78], transport reversal [92], registration methods [103], Wasserstein barycenters [39], Front Transport Reduction (FTR) [60], quadratic manifolds [43], or Transformed Generative Pre-Trained Physics-Informed Neural Networks (TGPT-PINN) [22]. Some of these proposed methods can be related to dynamical low-rank approximations [59, 98].

The LRNR architecture itself can be viewed as a deeper generalization of transported subspaces, a class of reduced models developed to overcome theoretical approximation bounds while enabling efficient computation through online-offline decomposition [93]. Their connection arises through what is called the inverse-bias trick [96]. In LRNRs, these ideas are further extended to higher dimensions using neural network architectures, which in turn generalize planar decompositions based on the Radon transform [90, 91]. Due to these connections to model reduction, the results in this work represent a substantial step forward in overcoming the Kolmogorov barrier. Nevertheless,

we note that certain high-dimensional hyperbolic problems were found to remain subject to other fundamental performance constraints [95].

In the general deep learning literature, there has been much interest in incorporating low-rankness in the model architecture both for better performance and better generalization: Introducing low rank factorizations of convolution kernels [56]; Widely known low rank adaptation (LoRA) techniques for large language models incorporate such techniques [54]; Modification of LoRA to physics-informed settings [74]; Low rank factorizations of components in the transformer model [35]. However, in these approaches specific components of the architecture (e.g. convolution kernels or the adaptation) are made low-rank, whereas the hidden states themselves are generally not low-rank. This is an important distinction from the LRNR architecture. The LRNR training approach is also distinct from train-then-truncate strategies considered in the past [24, 25].

### 2. Low Rank Neural Representation

In this section, we introduce the LRNR architecture. For a more extensive discussion of its motivation and derivation, we refer the reader to the theoretical work [96]. A more concise introduction, which is perhaps more useful for practitioners, appears in [27, 26].

2.1. The LRNR architecture. We first define feedforward neural networks (NNs) in a standard manner [36, 10]. Given the dimensions  $M_0, ... M_L \in \mathbb{N}$ , and an input  $\mathbf{x} \in \mathbb{R}^{M_0}$ , we define the corresponding output  $\mathbf{y} \in \mathbb{R}^{M_L}$  of the NN  $h(\mathbf{x}) = \mathbf{y} := \mathbf{z}^L$  by setting  $\mathbf{z}^0 := \mathbf{x}$  and computing the sequence  $(\mathbf{z}^\ell)$  via

(2.1) 
$$\mathbf{z}^{\ell} = \sigma(\mathbf{W}^{\ell}\mathbf{z}^{\ell-1} + \mathbf{b}^{\ell}) \in \mathbb{R}^{M_{\ell}} \quad \text{for } \ell = 1, \dots, L-1,$$
$$\mathbf{z}^{L} = \mathbf{W}^{L}\mathbf{z}^{L-1} + \mathbf{b}^{L} \in \mathbb{R}^{M_{L}}.$$

where  $\sigma$  is a nonlinear activation function,  $\mathbf{W}^{\ell} \in \mathbb{R}^{M_{\ell} \times M_{\ell-1}}$  and  $\mathbf{b}^{\ell} \in \mathbb{R}^{M_{\ell}}$ . Throughout, the superscript  $\ell$  is used as an index and not as an exponent.

We refer to a NN as an implicit neural representation (INR) if its inputs are spatio-temporal coordinates and the goal is to approximate a target spatio-temporal function. In our case, the inputs  $\mathbf{x} \in \mathbb{R}^d$  will be the spatial variables of the physical system, so the input dimension  $M_0$  is set as the spatial dimension  $M_0 := d$ . In particular, we are interested in representing a family of spatial functions, and to this end we consider a family of neural networks with a corresponding family of weights and biases. Suppose these weights and biases are determined by a set of coefficient variables represented by a vector  $\mathbf{s}$ ; then one may write

(2.2) 
$$\mathbf{W}^{\ell} = \mathbf{W}^{\ell}(\mathbf{s}), \qquad \mathbf{b}^{\ell} = \mathbf{b}^{\ell}(\mathbf{s}), \qquad h = h(\cdot; \mathbf{s}).$$

The distinguishing feature of a LRNR is the enforcement of a low-rank structure on the weights and biases. Consider enforcing a constraint that the family of weight matrices  $\{\mathbf{W}^{\ell}(\mathbf{s}) \mid \mathbf{s}\}$  and bias vectors  $\{\mathbf{b}^{\ell}(\mathbf{s}) \mid \mathbf{s}\}$ , defined over all coefficient parameters  $\mathbf{s}$ , share global column and row spaces of certain rank. A simple formulation would express  $\mathbf{W}^{\ell}(\mathbf{s})$  and  $\mathbf{b}^{\ell}(\mathbf{s})$  as

(2.3) 
$$\mathbf{W}^{\ell}(\mathbf{s}) = \sum_{i=1}^{r_1^{\ell}} s_{1,i}^{\ell} \mathbf{W}_i^{\ell}, \qquad \mathbf{b}^{\ell}(\mathbf{s}) = \sum_{i=1}^{r_2^{\ell}} s_{2,i}^{\ell} \mathbf{b}_i^{\ell},$$

where  $\mathbf{W}_i^{\ell}$  are rank-1 matrices and  $\mathbf{b}_i^{\ell}$  are basis vectors. More abstractly, we are imposing on the weights and biases the constraints

$$(2.4) \quad \dim \bigcup_{\mathbf{s}} \operatorname{colspan}(\mathbf{W}^{\ell}(\mathbf{s})), \dim \bigcup_{\mathbf{s}} \operatorname{rowspan}(\mathbf{W}^{\ell}(\mathbf{s})) \leqslant r_{1}^{\ell}, \quad \dim \bigcup_{\mathbf{s}} \operatorname{colspan}(\mathbf{b}^{\ell}(\mathbf{s})) \leqslant r_{2}^{\ell}.$$

This is the basic setup for the LRNR definition. The full definition of the LRNR architecture given below is modestly more general than what is given above: we allow  $\mathbf{W}_{i}^{\ell}$  to be sparse.

**Definition 2.1** (Low rank neural representation (LRNR)). A LRNR of depth L and rank  $\mathbf{r} \in \mathbb{R}^{2L}$  is a family of feedforward neural networks (2.1) whose layer-wise weights  $\mathbf{W}^{\ell}$  and biases  $\mathbf{b}^{\ell}$  depend on a set of coefficient variables  $\mathbf{s} \in \mathbb{R}^n$  with  $n = ||\mathbf{r}||_1$ . Denoting the individual entries of  $\mathbf{r}$  and  $\mathbf{s}$  using the indexing

$$(2.5) \mathbf{r} = (r_p^{\ell}: p = 1, 2; \ell = 1, \dots, L), \mathbf{s} = (s_{p,i}^{\ell}: p = 1, 2; i = 1, \dots, r_p^{\ell}; \ell = 1, \dots, L),$$

the s-dependent weights and biases are defined as

(2.6) 
$$\mathbf{W}^{\ell}(\mathbf{s}) = \sum_{i=1}^{r_1^{\ell}} s_{1,i}^{\ell} \mathbf{W}_i^{\ell} \in \mathbb{R}^{M_{\ell} \times M_{\ell-1}}, \qquad \mathbf{b}^{\ell}(\mathbf{s}) = \sum_{i=1}^{r_2^{\ell}} s_{2,i}^{\ell} \mathbf{b}_i^{\ell} \in \mathbb{R}^{M_{\ell}}, \qquad \ell = 1, 2, ..., L,$$

in which  $\mathbf{b}_i^{\ell}$  are given vectors, and each of  $\mathbf{W}_i^{\ell}$  is are either given rank-1 or sparse matrices. Furthermore, we

- denote by  $M := \max_{\ell} M_{\ell}$  the width of the network,
- define  $\mathcal{H}_{\mathbf{r},M}$  to be the collection of all LRNRs of depth L, rank  $\mathbf{r} \in \mathbb{R}^{2L}$ , and width M,
- $set \mathcal{H}_{\mathbf{r}} := \bigcup_{M} \mathcal{H}_{\mathbf{r},M}$ ,
- for each LRNR  $h \in \mathcal{H}_{\mathbf{r},M}$ , the specific NN corresponding to the coefficient values  $\mathbf{s}$  is denoted by  $h(\cdot;\mathbf{s})$ ,
- denote by  $\mathbf{s}_1^{\ell} \in \mathbb{R}^{r_1^{\ell}}$  the coefficients that appear in the weights in layer  $\ell$ , and  $\mathbf{s}_2^{\ell} \in \mathbb{R}^{r_2^{\ell}}$  the coefficients that appear in the biases in the layer  $\ell$ .

Given a LRNR  $h \in \mathcal{H}_{\mathbf{r},M}$ , suppose the corresponding  $(\mathbf{W}_i^{\ell})$  and  $(\mathbf{b}_i^{\ell})$  are learned first and are fixed. Then the full parameter state is encoded in the coefficient vector  $\mathbf{s}$ , which modulates the fixed weight and bias parameters. Thus we may identify the coefficient  $\mathbf{s}$  with a specific NN (or INR)  $h(\cdot;\mathbf{s})$ . The dimension of the coefficient vector  $\mathbf{s}$  is  $n = ||\mathbf{r}||_1$ . As discussed in the introduction, n is referred to as the coefficient count, and represents a type of expressiveness of LRNRs. For hyperbolic problems the existence of efficient LRNR approximations can be established rigorously, and this is the main topic of Sec. 3.

Def. 2.1 agrees with the LRNR definition given in [96] with a couple of generalizations. First, we allow the rank to be different for each weight and bias. Second, Def. 2.1 allows  $\mathbf{W}_i^{\ell}$  to be a sparse matrix: When  $\mathbf{W}_i^{\ell}$  in (2.3) is rank-1, it can be expressed as

(2.7) 
$$\mathbf{W}_{i}^{\ell} = \mathbf{u}_{i}^{\ell} \otimes \mathbf{v}_{i}^{\ell}, \quad \mathbf{u}_{i}^{\ell} \in \mathbb{R}^{M_{\ell}}, \quad \mathbf{v}_{i}^{\ell} \in \mathbb{R}^{M_{\ell-1}},$$

where  $\otimes$  denotes the outer product of two vectors. In [96] the operation  $\otimes$  was generalized to the Hadamard-Kronecker products  $\otimes_d : \mathbb{R}^{m_1} \times \mathbb{R}^{m_2} \to \mathbb{R}^{m_1 m_2 \times m_2}$  and  $d \otimes : \mathbb{R}^{m_1} \times \mathbb{R}^{m_2} \to \mathbb{R}^{m_1 \times m_1 m_2}$  between two vectors, defined as  $\mathbf{u} \otimes_d \mathbf{v} := \mathbf{u} \otimes \operatorname{diag}(\mathbf{v})$  and  $\mathbf{u}_d \otimes \mathbf{v} := \operatorname{diag}(\mathbf{u}) \otimes \mathbf{v}$  for vectors  $\mathbf{u} \in \mathbb{R}^{m_1}$  and  $\mathbf{v} \in \mathbb{R}^{m_2}$ . This enabled  $\mathbf{W}_i^\ell$  to be set as certain class of sparse matrices, e.g, the identity  $\mathbf{I} = \operatorname{diag}(\mathbf{u})_d \otimes \mathbf{v}$  when  $\mathbf{u}$  is taken to be a vector of ones and  $\mathbf{v}$  a 1-vector with a single entry of one. Here, we allow  $\mathbf{W}_i^\ell$  to be a general sparse matrix.

2.1.1. Implementation version. In our implementations, we work with the simpler version used in [27, 26]:  $\mathbf{W}_i^{\ell}$  is taken to be a rank-1 matrix (2.7). In this case, the weight matrix  $\mathbf{W}^{\ell}(\mathbf{s})$  can be rewritten in factored form,

$$(2.8) \mathbf{W}^{\ell}(\mathbf{s}) = \mathbf{U}^{\ell} \operatorname{diag}(\mathbf{s}_{1}^{\ell}) \mathbf{V}^{\ell \top}, \operatorname{with} \mathbf{U}^{\ell} := \left[\mathbf{u}_{1}^{\ell} \mid \cdots \mid \mathbf{u}_{r_{1}^{\ell}}^{\ell}\right], \mathbf{V}^{\ell} := \left[\mathbf{v}_{1}^{\ell} \mid \cdots \mid \mathbf{v}_{r_{1}^{\ell}}^{\ell}\right].$$

This simple version makes the weight matrix  $\mathbf{W}^{\ell}(\mathbf{s})$  resemble the factored form of singular value decompositions [27], but this factorized form of the weight matrix is distinct from the classical decomposition since the coefficients (the diagonal entries) are allowed to vary. The bias can also be written,

(2.9) 
$$\mathbf{b}^{\ell}(\mathbf{s}) = \mathbf{B}^{\ell}\mathbf{s}_{2}^{\ell} \quad \text{with} \quad \mathbf{B}^{\ell} := \left[\mathbf{b}_{1}^{\ell} \mid \dots \mid \mathbf{b}_{r_{2}^{\ell}}^{\ell}\right].$$

It is straightforward to see that, in this formulation, the output of the affine mapping at each layer

(2.10) 
$$\mathbf{z}^{\ell-1} \quad \mapsto \quad \mathbf{W}^{\ell}(\mathbf{s})\mathbf{z}^{\ell-1} + \mathbf{b}^{\ell}(\mathbf{s})$$

is a vector belonging to the column space of  $\mathbf{W}^{\ell}$  and  $\mathbf{b}^{\ell}$ , and therefore has rank at most  $r_1^{\ell} + r_2^{\ell}$ . It is also straightforward that the output from this mapping is stable with respect to  $\mathbf{z}^{\ell-1}$  and  $\mathbf{s}$ . Since the popular choice of nonlinear activation functions are Lipschitz continuous, this in turn implies the stability of the LRNR as a whole with respect to the inputs and the coefficients, as it is a composition of stable functions. In contrast, input instability is a well-known issue in standard

deep learning models [102, 13], and the high-rank weights incur these instabilities [94].

#### 3. Approximation results on LRNR coefficient counts

In this section, we provide approximation theoretical results regarding the LRNR coefficient counts, which imply the existence of efficient LRNR approximations of several important hyperbolic wave solutions.

3.1. The LRNR coefficient count. We defined the LRNR architecture in the previous section, and for a given LRNR of rank  $\mathbf{r} \in \mathbb{R}^{2L}$ , the total number of coefficients in  $\mathbf{s}$  (2.5) equals

(3.1) 
$$n = \|\mathbf{r}\|_1 = \sum_{p=1,2} \sum_{\ell=1}^L r_p^{\ell},$$

that is,  $r_1^{\ell}$  coefficients for the weight and  $r_2^{\ell}$  coefficients for the bias, across layers  $\ell = 1, ..., L$  (2.6). Following the discussion in the introduction, we define the notion of a LRNR coefficient count for a family of functions  $\mathcal{M}$  as the minimal number of coefficients needed for LRNRs in  $\mathcal{H}_{\mathbf{r},M}$  to attain certain approximation rates with respect to the width M.

**Definition 3.1** (LRNR coefficient count). Recall that  $\mathcal{H}_{\mathbf{r}}$  denotes the LRNRs of depth L, rank  $\mathbf{r} \in \mathbb{R}^{2L}$  and arbitrary width, and let  $\|\cdot\|$  be a norm over a Banach space  $\mathcal{X}$ . Given a family of functions  $\mathcal{M} \subset \mathcal{X}$ , let us define

(3.2) 
$$|\mathcal{M}|_{\mathcal{A}^{\alpha}(\mathcal{H}_{\mathbf{r}})} := \sup_{M} M^{\alpha} \inf_{h \in \mathcal{H}_{\mathbf{r},M}} \left( \sup_{u \in \mathcal{M}} \inf_{\mathbf{s} \in \mathbb{R}^{n}} ||u - h(\cdot; \mathbf{s})|| \right), \qquad n = ||\mathbf{r}||_{1}.$$

Then the LRNR coefficient count of  $\mathcal{M}$  is defined as

(3.3) 
$$\mathscr{C}(\mathcal{M}; \alpha) = \min \left\{ n \in \mathbb{N} \mid |\mathcal{M}|_{\mathcal{A}^{\alpha}(\mathcal{H}_{\mathbf{r}})} < \infty, n = ||\mathbf{r}||_{1} \right\}.$$

This definition relies on the commonly used notion of approximation spaces (see, e.g., [37]) and tests whether LRNRs with certain rank  $\mathbf{r}$ , which forms a special family of neural networks, can approximate a given collection of approximants  $\mathcal{M}$  with a standard approximation rate  $\alpha$  with respect to the width M.

Now, we bolster the viewpoint from the introduction that the LRNR architecture is inherently well-tailored for the task of approximating solutions to hyperbolic problems, by presenting some upper bounds for the coefficient counts of solutions to representative hyperbolic problems, namely the d-dimensional wave equation (Sec. 3.2), the d-dimensional advection equation (Sec. 3.3), and the 1-dimensional scalar conservation law (Sec. 3.4). Throughout this section, we set our activation as  $\sigma(\cdot) = (\cdot)_+$  the Rectified Linear Unit (ReLU).

3.2. The d-dimensional wave equation. Let us consider the constant-speed wave equation in dimension d. Let  $\Omega \subset \mathbb{R}^d$  denote a bounded domain with smooth  $C^1$  boundary, and  $\widehat{\Omega}$  denote the extended domain given by the Minkowski sum  $\widehat{\Omega} = \Omega + B(cT)$  with the open  $\ell_2$ -ball B(cT) of radius cT,

(3.4) 
$$\begin{cases} \partial_{tt} u - c^2 \Delta u = 0 \text{ in } \widehat{\Omega} \times (0, T) \\ u(\cdot, 0) = u_0 \text{ in } \widehat{\Omega}, & \text{where} \end{cases} \begin{cases} \text{const. } c > 0, \\ u_0 \in H^1(\widehat{\Omega}), \\ v_0 \in L^2(\widehat{\Omega}). \end{cases}$$

Here  $L^p(\Omega)$  denotes the Banach space induced by the  $L^p$ -norm  $\|\cdot\|_{L^p(\Omega)} = (\int_{\Omega} |\cdot|^p dx)^{1/p}$  for  $1 \leq p < \infty$ ,  $H^1(\Omega)$  denotes the Sobolev space whose weak derivative belong to  $L^2(\Omega)$  [40]. There is a unique solution  $u(\cdot,t) \in H^1(\Omega)$  for the smaller spatial domain  $\Omega \subset \widehat{\Omega}$  for  $t \in [0,T]$ , and the boundary effects can be ignored due to the finite propagation speed in wave equations [40], hence we omit the boundary conditions.

3.2.1. Motivation. We first motivate the key ideas through an informal discussion. Our result for the wave equation will be based on the fact that neural networks can be written as planar wave decompositions in the 2-layer case. For the given spatial input  $\mathbf{x} \in \mathbb{R}^d$ , a scalar-valued 2-layer neural network is of the form

(3.5) 
$$\mathbf{w}^{2} \cdot \sigma(\mathbf{W}^{1}x + \mathbf{b}^{1}) + b^{2} = \sum_{i=1}^{M} (w_{i}^{2}\sigma(\mathbf{w}_{i}^{1} \cdot \mathbf{x} + b_{i}^{1}) + b^{2}/M) = \sum_{i=1}^{M} g_{i}(\mathbf{w}_{i}^{1} \cdot \mathbf{x}),$$

where we define the scalar 1d functions  $g_i : \mathbb{R} \to \mathbb{R}$  as  $g_i(\beta) := w_i^2 \sigma(\beta + \hat{b}_i^1) + b^2/M$  for i = 1, ..., M. We will describe how, the solution u of (3.4) can be represented as a LRNR using this decomposition. For the sake of exposition, suppose we are given an initial condition that has precisely the form in (3.5) with zero velocity, that is,

(3.6) 
$$u_0(\mathbf{x}) = \sum_{i=1}^M g_i(\mathbf{w}_i^1 \cdot \mathbf{x}), \quad \mathbf{w}_i^1 \in S^{d-1}, \qquad v_0 \equiv 0.$$

Considering the individual terms in the sum, the application of the multidimensional Laplacian reduces to a single dimensional one,

(3.7) 
$$\Delta g_i(\mathbf{w}_i^1 \cdot \mathbf{x}) = |\mathbf{w}_i^1|^2 g_i''(\mathbf{w}_i^1 \cdot \mathbf{x}) = g_i''(\mathbf{w}_i^1 \cdot \mathbf{x}).$$

Hence, the solution to the wave operator  $(\partial_{tt} - c^2 \Delta)$  in (3.4), when applied to each planar function  $g_i(\beta)$ , can be written as the 1d wave operator  $(\partial_{tt} - c^2 \partial_{\beta\beta})$ . As a result, the d'Alembert solution  $\frac{1}{2}(g_i(\beta - ct) + g_i(\beta + ct))$  solves the 1d wave equation with the initial condition  $g_i(\beta)$ . By linearity, we arrive at the solution

(3.8) 
$$u(\mathbf{x},t) = \frac{1}{2} \sum_{i=1}^{M} \left[ g_i(\mathbf{w}_i^1 \cdot \mathbf{x} - ct) + g_i(\mathbf{w}_i^1 \cdot \mathbf{x} + ct) \right].$$

This representation is closely related to the Lax-Phillips representation in odd dimensions [65] and is the basis for Radon transform-based techniques [15, 90, 91, 72]. Inserting the 2-layer form of  $g_i$  we have assumed in (3.5), the explicit form of the solution (3.8) can be rewritten as a LRNR,

(3.9) 
$$u(\mathbf{x},t) = \frac{1}{2} \sum_{i=1}^{M} \left[ w_i^2 \sigma((\mathbf{w}_i^1 \cdot \mathbf{x}) + b_i^1 - ct) + b^2 / M + w_i^2 \sigma((\mathbf{w}_i^1 \cdot \mathbf{x}) + b_i^1 + ct) + b^2 / M \right]$$
$$= \widehat{\mathbf{w}}^2 \cdot \sigma(\widehat{\mathbf{W}}^1 x + \widehat{\mathbf{b}}^1(\mathbf{s}(t))) + \widehat{b}^2,$$

where only the first bias term  $\hat{\mathbf{b}}^1$  is dependent on t. Focusing on this bias term, we write it as a function of its coefficients  $\hat{\mathbf{b}}^1(\mathbf{s}(t))$ : Once we let

(3.10) 
$$\mathbf{B}^{1} := \begin{bmatrix} \vdots & \vdots \\ b_{i}^{1} & -c \\ b_{i}^{1} & c \\ \vdots & \vdots \end{bmatrix},$$

the bias  $\mathbf{b}^1(\mathbf{s}(t))$  is seen to be a linear combination of the two column vectors of  $\mathbf{B}^1$  with the coefficients

(3.11) 
$$\hat{\mathbf{b}}^1(\mathbf{s}(t)) = \mathbf{B}^1 \mathbf{s}_2^1(t), \quad s_{2,1}^1(t) \equiv 1, \quad s_{2,2}^1(t) = t.$$

Thus, the neural network can be expressed a LRNR with  $r_2^1 = 2$ .

3.2.2. LRNR coefficient count for the d-dimensional wave equation. We now turn to a formal statement and its proof. We define the Barron space  $\mathcal{B}$  [38] as the collection of functions with finite Barron norm  $\|\cdot\|_{\mathcal{B}_k}$  for  $k \in \mathbb{N}_0$  is given by

$$(3.12) \|f\|_{\mathcal{B}_k} := \inf_{\rho \in P_f} \mathbb{E}\left[|a|\left(\|\mathbf{w}\|_1 + |b|\right)\right] \text{ where } P_f = \left\{\rho : f(\mathbf{x}) = \int a\sigma^k(\mathbf{w} \cdot \mathbf{x} + b)\rho(\mathrm{d}a, \mathrm{d}\mathbf{w}, \mathrm{d}b)\right\}.$$

If the initial conditions in (3.4) are in Barron spaces, one can bound the LRNR coefficient count, and the rate  $\alpha$  is provided by existing approximation theoretical results.

**Theorem 3.2** (Wave equation in d dimensions). Suppose u is the solution to the d-dimensional wave equation (3.4) where  $u_0 \in \mathcal{B}_1$  and  $v_0 \in \mathcal{B}_0$ . Then for the collection  $\mathcal{M} := \{u(\cdot, t)|_{\Omega} \mid t \in [0, T]\}$ ,

(a) there is a LRNR approximation  $u_M \in \mathcal{H}_{\mathbf{r},M}$  with depth L=2 and rank  $\mathbf{r}=(d,2;1,0)$  whose coefficients  $\mathbf{s}$  depend on t such that

(3.13) 
$$\|u_{M}(\cdot; \mathbf{s}(t)) - u(\cdot, t)\|_{H^{1}(\Omega)} \lesssim M^{-\frac{1}{2} - \frac{1}{2d}} \left( \|u_{0}\|_{\mathcal{B}_{1}} + \|v_{0}\|_{\mathcal{B}_{0}} \right),$$

$$\|\partial_{t} u_{M}(\cdot; \mathbf{s}(t)) - \partial_{t} u(\cdot, t)\|_{L^{2}(\Omega)} \lesssim M^{-\frac{1}{2} - \frac{1}{2d}} \left( \|u_{0}\|_{\mathcal{B}_{1}} + \|v_{0}\|_{\mathcal{B}_{0}} \right),$$

(b) the LRNR coefficient count  $\mathscr{C}$  for  $\mathcal{M}$  satisfies the upper bound,

(3.14) 
$$\mathscr{C}\left(\mathcal{M}; \alpha = \frac{1}{2} + \frac{1}{2d}\right) \leqslant d + 3.$$

*Proof.* As the initial data  $u_0$  and  $v_0$  lie in the Barron spaces  $\mathcal{B}_1$  and  $\mathcal{B}_0$ , respectively, they can be written

(3.15) 
$$u_0(x) = \int a\sigma(\mathbf{w} \cdot \mathbf{x} + b) d\mu(da, d\mathbf{w}, db), \quad v_0(x) = \int a\sigma^0(\mathbf{w} \cdot \mathbf{x} + b) d\nu(da, d\mathbf{w}, db),$$

with respective optimal measures  $\mu$  and  $\nu$ . Here  $\sigma^0$  is the derivative of the ReLU, the jump function. Thanks to this planar wave decomposition the solution to the wave equation with this initial condition is given by (see Sec. A or [41, Sec. 5.F])

(3.16) 
$$u(\mathbf{x},t) = U(\mathbf{x},t) + V(\mathbf{x},t),$$

$$U(\mathbf{x},t) = \frac{1}{2} \int a \left[ \sigma(\mathbf{w} \cdot \mathbf{x} + b - ct) + \sigma(\mathbf{w} \cdot \mathbf{x} + b + ct) \right] d\mu(\mathrm{d}a, \mathrm{d}\mathbf{w}, \mathrm{d}b),$$

$$V(\mathbf{x},t) = \frac{1}{2} \int a \left[ \sigma(\mathbf{w} \cdot \mathbf{x} + b - ct) + \sigma(\mathbf{w} \cdot \mathbf{x} + b + ct) \right] d\nu(\mathrm{d}a, \mathrm{d}\mathbf{w}, \mathrm{d}b).$$

To obtain a neural network representation, we employ Maurey sampling [87, 75, 100]: There are  $a_i$ ,  $w_i$  and  $b_i$  for  $i = 1, ..., m_1$  and  $i = m_1 + 1, ..., m_1 + m_2$ , respectively so that the sums

(3.17) 
$$u_{0,m_1}(\mathbf{x}) = \sum_{i=1}^{m_1} a_i \sigma(\mathbf{w}_i \cdot \mathbf{x} + b_i), \quad v_{0,m_2}(\mathbf{x}) = \sum_{i=m_1+1}^{m_1+m_2} a_i \sigma'(\mathbf{w}_i \cdot \mathbf{x} + b_i),$$

approximate the initial conditions in  $\widehat{\Omega}$ ,

and the constants depend on  $\sigma$ , d and the respective choices of error norms.

Letting  $M := 2(m_1 + m_2)$ , the solution with the approximate initial conditions (3.17) can be written in the form of (3.16), as a sum of Dirac measures, resulting in the discrete analogue

$$(3.19) u_{M}(\mathbf{x},t) = U_{m_{1}}(x,t) + V_{m_{2}}(x,t),$$

$$U_{m_{1}}(\mathbf{x},t) = \frac{1}{2} \sum_{i=1}^{m_{1}} a_{i} \left[ \sigma(\mathbf{w}_{i} \cdot \mathbf{x} + b_{i} - ct) + \sigma(\mathbf{w}_{i} \cdot \mathbf{x} + b_{i} + ct) \right],$$

$$V_{m_{2}}(\mathbf{x},t) = \frac{1}{2} \sum_{i=m_{1}+1}^{m_{1}+m_{2}} a_{i} \left[ \sigma(\mathbf{w}_{i} \cdot \mathbf{x} + b_{i} - ct) + \sigma(\mathbf{w}_{i} \cdot \mathbf{x} + b_{i} + ct) \right].$$

Due to linearity, the difference  $u_M - u$  between the approximate and exact solutions satisfies the wave equation. Using the energy estimates, we now show that  $u_M - u$  remains small over time.

The energy E(t) over the cone  $\widehat{\Omega}_t := \Omega + B(c(T-t))$  reads

(3.20) 
$$E(t) := \frac{1}{2} |u_M(\cdot, t) - u(\cdot, t)|_{H^1(\widehat{\Omega}_t)}^2 + \frac{1}{2} ||\partial_t u_M(\cdot, t) - \partial_t u(\cdot, t)||_{L^2(\widehat{\Omega}_t)}^2,$$

and satisfies  $E'(t) \leq 0$  for  $t \in [0,T]$  (a standard energy estimate; see for example [40, Sec. 2.4]) hence

(3.21) 
$$E(t) \leq E(0) \leq m_1^{-1 - \frac{1}{d}} \|u_0\|_{\mathcal{B}_1}^2 + m_2^{-1 - \frac{1}{d}} \|v_0\|_{\mathcal{B}_0}^2, \quad t \in [0, T].$$

With an application of a Poincaré-Friedrichs inequality in time, one bounds the  $L^2$ -norm

Pulling these estimates together,

$$\|u_{M}(\cdot,t) - u(\cdot,t)\|_{H^{1}(\Omega)}^{2} + \|\partial_{t}u_{M}(\cdot,t) - \partial_{t}u(\cdot,t)\|_{L^{2}(\Omega)}^{2}$$

$$\leq \|u_{M}(\cdot,t) - u(\cdot,t)\|_{H^{1}(\widehat{\Omega}_{t})}^{2} + \|\partial_{t}u_{M}(\cdot,t) - \partial_{t}u(\cdot,t)\|_{L^{2}(\widehat{\Omega}_{t})}^{2}$$

$$\leq \|u_{M}(\cdot,t) - u(\cdot,t)\|_{L^{2}(\widehat{\Omega}_{t})}^{2} + E(t)$$

$$\leq \|u_{M}(\cdot,0) - u(\cdot,0)\|_{L^{2}(\widehat{\Omega}_{t})}^{2} + E(0)$$

$$\leq m_{1}^{-1-\frac{1}{d}} \|u_{0}\|_{\mathcal{B}_{1}}^{2} + m_{2}^{-1-\frac{1}{d}} \|v_{0}\|_{\mathcal{B}_{0}}^{2}$$

$$\leq M^{-1-\frac{1}{d}} \left( \|u_{0}\|_{\mathcal{B}_{1}}^{2} + \|v_{0}\|_{\mathcal{B}_{0}}^{2} \right) .$$

So we arrive at the uniform error estimate for  $t \in [0, T]$ ,

(3.24) 
$$\|u_{M}(\cdot,t) - u(\cdot,t)\|_{H^{1}(\Omega)} \lesssim M^{-\frac{1}{2} - \frac{1}{2d}} \left( \|u_{0}\|_{\mathcal{B}_{1}} + \|v_{0}\|_{\mathcal{B}_{0}} \right),$$

$$\|\partial_{t}u_{M}(\cdot,t) - \partial_{t}u(\cdot,t)\|_{L^{2}(\Omega)} \lesssim M^{-\frac{1}{2} - \frac{1}{2d}} \left( \|u_{0}\|_{\mathcal{B}_{1}} + \|v_{0}\|_{\mathcal{B}_{0}} \right),$$

and the suppressed constants depend on  $\sigma, d, T$  and on the choice of error norms. This proves (a).

Now we reformulate the approximation  $u_M$  in the form of a LRNR. Combining all weights into vectors and matrices  $\mathbf{a} \in \mathbb{R}^M$ ,  $\mathbf{W} \in \mathbb{R}^{M \times d}$ , and  $\mathbf{b} \in \mathbb{R}^M$ , we obtain

(3.25) 
$$u_M(\mathbf{x},t) = \frac{1}{2c} \mathbf{a} \, \sigma \left( \mathbf{W} \mathbf{x} + \mathbf{b} + ct \begin{bmatrix} +1 \\ -1 \end{bmatrix} \right).$$

With a slight abuse of notation, we rewrite this as a LRNR with time-dependent coefficients s(t) of width M and depth L=2

(3.26) 
$$u_M(\mathbf{x}; \mathbf{s}(t)) = \underbrace{\frac{1}{2c}}_{\mathbf{W}^2} \sigma \left( \underbrace{\mathbf{W}}_{\mathbf{W}^1} \mathbf{x} + \underbrace{\begin{bmatrix} \mathbf{b} & c\mathbf{1} \\ -c\mathbf{1} \end{bmatrix}}_{\mathbf{B}^1} \underbrace{\begin{bmatrix} 1 \\ t \end{bmatrix}}_{\mathbf{s}_2^1(t)} \right).$$

The weight matrices  $\mathbf{W}^1$  and  $\mathbf{W}^2$  are fixed, hence their rank is equal to the usual rank of these matrices,

(3.27) 
$$r_1^1 = \text{rank}(\mathbf{W}^1) \le d, \qquad r_1^2 = \text{rank}(\mathbf{W}^2) = 1,$$

and  $\mathbf{b}^2 \equiv 0$ , so we have  $r_2^2 = 0$ . So the rank of this LRNR is at most

(3.28) 
$$\mathbf{r} = (r_1^1, r_2^1; r_1^2, r_2^2) = (d, 2; 1, 0),$$

hence the coefficient count is at most  $n = ||\mathbf{r}||_1 = d+3$ , for the norm  $H^1(\Omega)$  and the rate  $\alpha = \frac{1}{2} + \frac{1}{2d}$ . This proves (b).

3.3. **The** *d***-dimensional advection equation.** Similar bounds can be obtained for the constant-speed advection equation.

**Theorem 3.3** (Advection equation in d dimensions). Let  $\widehat{\Omega}$  and  $\Omega$  be as in (3.4), and let u be the solution to the advection equation posed in  $\widehat{\Omega}$ 

(3.29) 
$$\begin{cases} \hat{c}_t u + \mathbf{a} \cdot \nabla u = 0 \text{ in } \widehat{\Omega}, \\ u(\cdot, 0) = u_0 \text{ in } \widehat{\Omega}, \end{cases} \text{ with } \|\mathbf{a}\|_2 = c, \text{ and } u_0 \in L^2(\widehat{\Omega}).$$

If  $u_0 \in \mathcal{B}_1$  then for the collection  $\mathcal{M} := \{u(\cdot, t) \mid t \in [0, T]\}$  the LRNR coefficient count  $\mathscr{C}$  satisfies the upper bound

(3.30) 
$$\mathscr{C}\left(\mathcal{M}; \alpha = \frac{1}{2} + \frac{1}{2d}\right) \leqslant d + 3.$$

where the underlying error norm is  $\|\cdot\|_{L^2(\Omega)}$ .

*Proof.* The proof is very similar to that of Theorem 3.2, therefore we omit it.

3.4. The 1d scalar conservation laws. A notable recent result is that deeper LRNRs can efficiently handle arbitrary shock interactions in nonlinear scalar conservation laws. This result can be rephrased in terms of the coefficient count.

**Theorem 3.4** (1d scalar conservation laws). Let u be the solution to the scalar conservation law posed on the unit interval  $\Omega := (0,1)$  for a given smooth flux  $F \in C^{\infty}(\mathbb{R})$  that is convex F'' > 0,

(3.31) 
$$\begin{cases} \partial_t u + \partial_x F(u) = 0 & \text{in } \Omega \times (0, T), \\ u(\cdot, 0) = u_0. \end{cases}$$

with compactly supported initial condition  $u_0 \in BV(\Omega)$  and final time T small enough so  $u(\cdot,t)$  is compactly supported in  $\Omega$  for  $t \in [0,T]$ . For the collection  $\mathcal{M} := \{u(\cdot,t) \mid t \in [0,T]\}$  the LRNR coefficient count  $\mathscr{C}$  satisfies the upper bound

(3.32) 
$$\mathscr{C}\left(\mathcal{M}; \alpha = \frac{1}{2}\right) \leqslant 12,$$

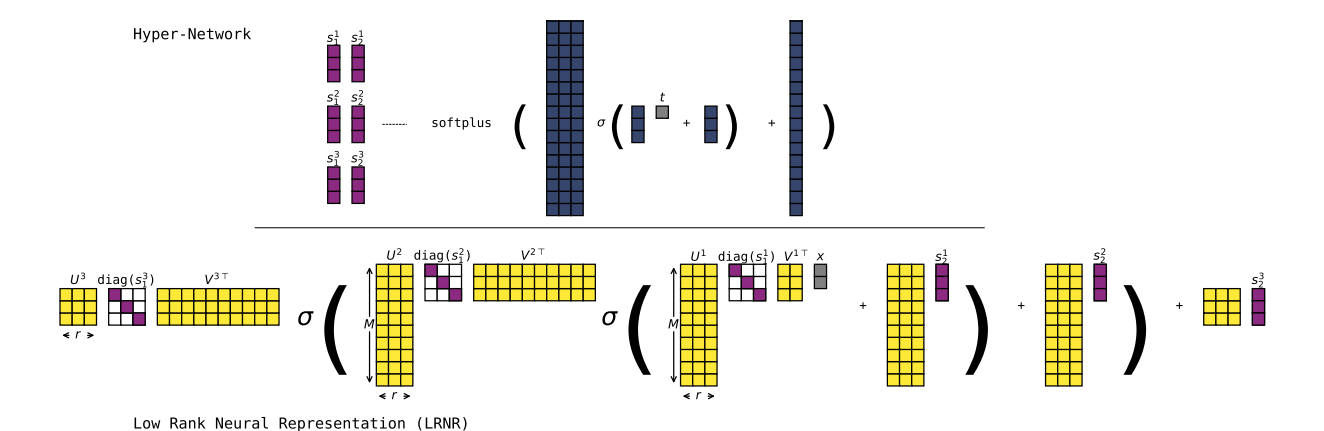


FIGURE 2. A diagram depicting the hypernetwork and the low rank neural representation. The hypernetwork takes the time variable t as input, and outputs the coefficients s (2.5) which are used as the highlighted entries to generate the LRNR weights and biases. In this example, the input dimension is two, the output dimension is three, and the rank is three.

where the underlying error norm is  $\|\cdot\|_{L^1(\Omega)}$ .

*Proof.* Recalling the LRNR construction used in the main theorem from [96], there exists a LRNR  $u_M \in \mathcal{H}_{\mathbf{r},M}$  with number of layers L = 5 and  $\mathbf{r} = (1, 2, 1, 1, 1; 1, 1, 2, 2, 0)$  such that

(3.33) 
$$||u(\cdot,t)-u_M(\cdot,t)||_{L^1(\Omega)} \lesssim M^{-\frac{1}{2}} |u_0|_{TV} (1+|u_0|_{TV}) (1+T||F''||_{L^{\infty}(u_0(\Omega))}), \quad t \in [0,T]$$
 where  $u_M$  has width  $M$ . So we have LRNR coefficient count  $n = ||\mathbf{r}||_1 = 12$  with rate  $\alpha = \frac{1}{2}$ .  $\square$ 

Hence, these theoretical constructions prove that efficient representations of complicated wave phenomena exist. This naturally leads to the computational question of whether such efficient representations can be learned directly from data: The rest of this work reports results in the positive.

### 4. Data-driven meta-learning framework for wave problems

In this section, the hypernetwork framework and the precise training methods are discussed. In previous works [27, 26], the meta-learning with a hypernetwork approach was shown to be effective in the physics-informed neural networks setting. Here, we investigate the effectiveness of a similar framework in a data-driven setting.

We will use a LRNR of depth L and rank  $\mathbf{r} \in \mathbb{R}^{2L}$  given in Def. 2.1 with the choice of rank-1 matrices in (2.7). The hypernetwork approach [48] employs an auxiliary neural network called the hypernetwork to generate the weights and biases of an INR. In our case, only the coefficient variables will be output from the hypernetwork. We set our hypernetwork  $f_{\text{hyper}}$  to output the coefficients  $\mathbf{s} \in \mathbb{R}^n$  (with  $n = ||\mathbf{r}||_1$ ), and since we are interested in the dynamics, we set the hypernetwork to take as input the time variable t. That is,

(4.1) 
$$f_{\text{hyper}}(t) = \mathbf{s}, \quad t \in [0, T], \quad \mathbf{s} \in \mathbb{R}^n,$$

and the resulting coefficients s (2.5) are used as coefficients in the low-rank weight and bias expansions (2.6).

The LRNR and the hypernetwork together form a meta-network, defined as the concatenation of a hypernetwork and a LRNR: A diagram depicting the meta-network is given in Fig. 2.

Recall that the coefficient vector  $\mathbf{s}$  (2.5) consists of entries  $\mathbf{s}_{1,i}^{\ell}$  and  $\mathbf{s}_{2,i}^{\ell}$ , where  $\mathbf{s}_{1,i}^{\ell}$  denotes the *i*-th coefficient for the weight matrix in layer  $\ell$ , used as the diagonal entries in the SVD-like factored form (2.8), and  $\mathbf{s}_{2,i}^{\ell}$  denotes the *i*-th coefficient for the bias in layer  $\ell$ , used to scale the basis vectors  $\mathbf{b}_{i}^{\ell}$  (2.9). Aside from the coefficients  $\mathbf{s}$ , the LRNR formulation has the  $\mathbf{s}$ -independent parameters  $\mathbf{U}^{\ell}$ ,  $\mathbf{V}^{\ell}$  (2.8) and  $\mathbf{B}^{\ell}$  (2.9). Collecting all of these, the entirety of  $\mathbf{s}$ -independent parameters is

(4.2) 
$$\mathbf{U} = (\mathbf{U}^{\ell})_{\ell=1}^{L}, \quad \mathbf{V} = (\mathbf{V}^{\ell})_{\ell=1}^{L}, \quad \mathbf{B} = (\mathbf{B}^{\ell})_{\ell=1}^{L}.$$

It remains to choose the dimensions of these matrices: We choose the same width across all layers  $M_{\ell} \equiv M$  for  $\ell = 1, ..., L-1$  for simplicity.

With this notation, we may write the LRNR as a function of the spatio-temporal input, parameterized by **U**, **V**, **B** (which are independent of **s**) and the coefficients **s**:

$$(4.3) h(\bullet; \mathbf{U}, \mathbf{V}, \mathbf{B}, \mathbf{s}).$$

Next, we denote by  $\Theta$  the parameters of the hypernetwork  $f_{\text{hyper}}: \mathbb{R} \to \mathbb{R}^n$ 

$$(4.4) f_{\text{hyper}}(\bullet; \Theta).$$

The meta-network is then the concatenation

$$(4.5) h(\bullet; \mathbf{U}, \mathbf{V}, \mathbf{B}, f_{\text{hyper}}(\bullet; \mathbf{\Theta})),$$

which can be interpreted as a larger feedforward neural network with parameters **U**, **V**, **B**, and **Θ**. We emphasize that the key distinction between this formulation and other proposals is that the hypernetwork outputs only the coefficients **s**, as opposed to outputting all entries of the weights and biases as in SIREN [101] or NIF [83]. The hypernetwork outputs coefficients **s** which are then multiplied by the matrices in **U**, **V**, **B** that remain constant, thus the variation in the weights and biases are restricted so as to preserve low-rankness in the sense of (2.8-2.9). In generic hypernetwork approaches like the SIREN hypernetwork approach [101], it is technically possible for a generic hypernetwork (that outputs all parameters) to discover specific parameters satisfying this particular inductive bias during training; in practice this was found to be unlikely in our experiments. In the NIF approach the variation is not independent across layers due to the bottleneck structure in the output of the hypernetwork; thus it is not possible for the NIF approach [83] to discover the low-rank structure of a LRNR in its general form. We note, however, that one example given in the paper introducing NIF appears to implicitly exploit the LRNR structure, due to the choice of small width that indirectly induces the weights to be low-rank (see the first figure of Fig. 3 in [83]).

For training, we use standard misfit cost functions, with the exception that we normalize them as follows:

(4.6) 
$$\mathcal{L}_{\text{misfit}}(\widehat{\mathbf{y}}, \mathbf{y}; q) := \frac{\|\widehat{\mathbf{y}} - \mathbf{y}\|_q^q}{\|\mathbf{y}\|_q^q}.$$

Throughout, we use q = 1 or q = 2, corresponding to normalized versions of  $\ell_1$  loss and Mean Squared Error (MSE), respectively.

4.1. Sparsity promoting regularizer and orthogonality constraints. A standard optimization using only the misfit function (4.6) and a PINNs penalty was shown to be effective in the first work that introduced the hypernetwork approach for LRNRs [27]. However, the trained LRNRs did not necessarily exhibit a low-rank structure. In the analogy between (2.8) and the singular value decomposition (SVD), low-rankness would correspond to the property (2.4-??) holding for a small r. However, the coefficients (2.5) that were output from the hypernetwork did not exhibit strong decay with respect to the index i, requiring r to be roughly on the same scale as the width M. A straightforward approach to inducing low-rankness in this case will be to introduce shrinkage, for example a simple  $\ell_1$  regularizer, intended to promote sparsity. However, in our experiments, this approach was not effective in inducing sparsity in the coefficient variables. We attribute this

phenomenon to the fact that the coefficients, now playing the role of singular values in (2.8), vary with time; so the dominant values also change.

This motivated the sparsity-promoting regularizer introduced in [26], which penalizes non-decay while relaxing it to allow a sparse violation of the penalty. It is given by

(4.7) 
$$\mathcal{R}_{\text{sparse}}(\mathbf{s}; \gamma) := \sum_{\ell=1}^{L} \sum_{p=1,2} \| (\mathbf{\Gamma}(\gamma) \mathbf{s}_{p}^{\ell})_{+} \|_{\ell^{1}}, \qquad \mathbf{\Gamma}(\gamma) = \begin{bmatrix} -1 & \gamma & & \\ & -1 & \gamma & \\ & & \ddots & \ddots \\ & & & -1 & \gamma \end{bmatrix}.$$

This regularizer does not directly promote sparsity in s, but instead encourages sparsity in the transformed vector

$$\left( (\gamma s_{p,j+1}^{\ell} - s_{p,j}^{\ell})_{+} \right)_{j}$$

for each p and  $\ell$ . We incorporate this regularizer into our loss function.

We also apply soft orthogonality constraints to the vectors involved in the rank-1 matrix expansions,

$$(4.9) \mathcal{R}_{\text{ortho}}(\mathbf{U}, \mathbf{V}, \mathbf{B}) := \sum_{\ell=1}^{L} \left( \frac{1}{\# \mathbf{U}^{\ell}} \| \mathbf{U}^{\ell \top} \mathbf{U}^{\ell} - \mathbf{I} \|_{F}^{2} + \frac{1}{\# \mathbf{V}^{\ell}} \| \mathbf{V}^{\ell \top} \mathbf{V}^{\ell} - \mathbf{I} \|_{F}^{2} + \frac{1}{\# \mathbf{B}^{\ell}} \| \mathbf{B}^{\ell \top} \mathbf{B}^{\ell} - \mathbf{I} \|_{F}^{2} \right)$$

where  $\|\cdot\|_F$  denotes the Frobenius norm, and # indicates the number of entries in a matrix. In our experiments, the inclusion of the orthogonality penalty consistently improved the training loss decay.

Finally, our training loss function is obtained by adding the regularizers (4.9-4.7) to the misfit loss function,

(4.10) 
$$\mathcal{L}(\mathbf{U}, \mathbf{V}, \mathbf{B}, \mathbf{\Theta}) := \mathbb{E}_{x,t} \left[ \mathcal{L}_{\text{misfit}}(u(\mathbf{x}; \mathbf{U}, \mathbf{V}, \mathbf{B}, f_{\text{hyper}}(t; \mathbf{\Theta})), u_{\text{data}}(\mathbf{x}, t)) \right] \\ + \lambda_{\text{sparse}} \mathcal{R}_{\text{sparse}}(f_{\text{hyper}}(t)) + \lambda_{\text{ortho}} \mathcal{R}_{\text{ortho}}(\mathbf{U}, \mathbf{V}, \mathbf{B}).$$

We use the Adam optimizer [58] to minimize the loss. The hyperparameters  $\lambda_{\text{sparse}}$  and  $\lambda_{\text{ortho}}$ , which control the strength of the regularization terms, and the architecture hyperparameters M, r, and L of the LRNR, are tuned using random search among a set of feasible choices, as implemented in the Ray Tune package [70].

- 4.2. Mollifiers, adaptive sampling, and misfit switch. We introduce several techniques to handle challenges in training the model with the loss (4.10).
- 4.2.1. *Mollifiers*. Due to the sharp jumps present in our compressible Euler example, standard training methods for INRs are not effective. For instance, we implemented the hypernetwork approach using SIREN, where a similar training procedure was applied except that the INR was a standard (non-low-rank) neural network, and the hypernetwork outputs all of the weights and biases of the NN in (2.1) (these results are discussed in Sec. 4.3).

To alleviate this difficulty in examples with a single spatial dimension d = 1, we mollify the data by convolving the uniformly sampled spatial data with a box function. We initialize the width of the support of the box function and decrease it according to a schedule over the course of training epochs:

(4.11) 
$$\mathcal{L}_{\text{misfit}}\left(u(\mathbf{x}; \mathbf{U}, \mathbf{V}, \mathbf{B}, f_{\text{hyper}}(t; \mathbf{\Theta})), (\chi_w * u_{\text{data}})(\mathbf{x}, t)\right),$$

where  $\chi_w$  is a d-dimensional box function defined as  $\chi_w := \frac{1}{(2w)^d} \prod_{i=1}^d \mathbb{1}_{[-w,w]}(x_i)$ .

The convolved function is a smeared-out version of the original, making it easier to fit using gradient descent-based algorithms [88, 4, 113]. We initialize the mollifier radius  $w_0$  as a user-specified hyperparameter, and at epoch  $i_{\text{epc}}$ , contract the radius using a linear decay schedule:

$$(4.12) w_{i_{\text{epc}}} = w_0 \left( \frac{n_{\text{epc}} - 2i_{\text{epc}}}{n_{\text{epc}}} \right)_+,$$

so that the radius vanishes halfway through the allocated number of epochs. This strategy is a form of numerical continuation [68] or curriculum learning [2, 5].

- 4.2.2. Adaptive sampling. Another approach we deploy to resolve sharp discontinuities in the data is to use adaptive spatial sampling. Adaptive mesh refinement (AMR) codes such as Clawpack are designed to produce adaptive samples that concentrate near sharp features. In higher spatial dimensions, using AMR-generated data yielded superior results compared to applying mollifiers.
- 4.2.3. Misfit switch. We also choose the misfit loss adaptively. Taking the weighted misfit

(4.13) 
$$\mathcal{L}_{\text{misfit}}(\bullet) := \alpha \mathcal{L}_{\text{misfit}}(\bullet; q = 1) + (1 - \alpha) \mathcal{L}_{\text{misfit}}(\bullet; q = 2)$$

we switch from MSE to  $\ell_1$  loss whenever a predefined threshold  $\tau$  is reached by starting with  $\alpha = 0$  then setting  $\alpha = 1$  in the first epoch in which  $\mathcal{L}_{\text{misfit}} < \tau$ , and reset the learning rate. This strategy is motivated by the observation that MSE loss often results in persistent Gibbs-like oscillations when approximating sharp jump discontinuities, whereas  $\ell_1$  loss tends to yield more accurate reconstructions. The approach is further supported by the  $L_1$  minimization formulation of convective problems [47, 46]. It is a form of multi-objective weighting [23, 112, 52, 105, 106], although the switch is applied instantaneously. The threshold  $\tau$  is determined heuristically through preliminary training runs without switching, and is set slightly above the best MSE misfit loss attained in those runs.

- 4.3. **Training results.** We report our training results below. Four representative examples are considered, each exhibiting characteristic behaviors of hyperbolic systems: the 1d compressible Euler equations (Woodward-Colella shock collision problem [111, 110, 67]); the 2d acoustics equations with periodic boundary conditions; the 2d Burgers equation with periodic boundary conditions; and the 2d advection equation with time-dependent, spatially varying advection velocities. For each example, we use PDE solution data consisting of 81 equally spaced time samples, generated using the Clawpack software package [28]. See Fig. 3 for the solution plots displaying the data.
- 4.3.1. 1d Compressible Euler example: Woodward-Colella problem. We show the training results for the 1d Euler example. Fig. 6 displays the training loss, regularization terms, mollifier radius, and learning rate over time. The threshold for switching from the (normalized) MSE loss to the (normalized)  $\ell_1$  loss was set to  $5 \times 10^{-4}$ . This threshold is reached quickly, and it was observed that mollifying the data facilitates reaching the threshold more efficiently via gradient descent. Once the misfit loss switches (4.13), the mollifier radius continues to decrease linearly according to the prescribed schedule (4.12). Each reduction in radius causes a temporary increase in loss due to the instantaneous change in the data, but subsequent gradient descent iterations reduce the loss again.

During epochs approximately from 3K to 40K, there is a visible competition between the increasing tendency of the  $\ell_1$  loss whenever the mollifier radius is decreased, and the decreasing tendency due to gradient descent. After this transition period, the mollification is fully phased out, and continued training with the standard  $\ell_1$  loss leads to further improvement in data fitting. Note that the MSE loss corresponds to the square of the  $\ell_2$  loss. Thus, a threshold value of  $5 \times 10^{-4}$  for the MSE loss roughly corresponds to an  $\ell_2$  loss of 0.02 after taking the square root. As a result, the apparent change in loss and accuracy at the switching point (marked by the vertical red line) is visually exaggerated in this plot.

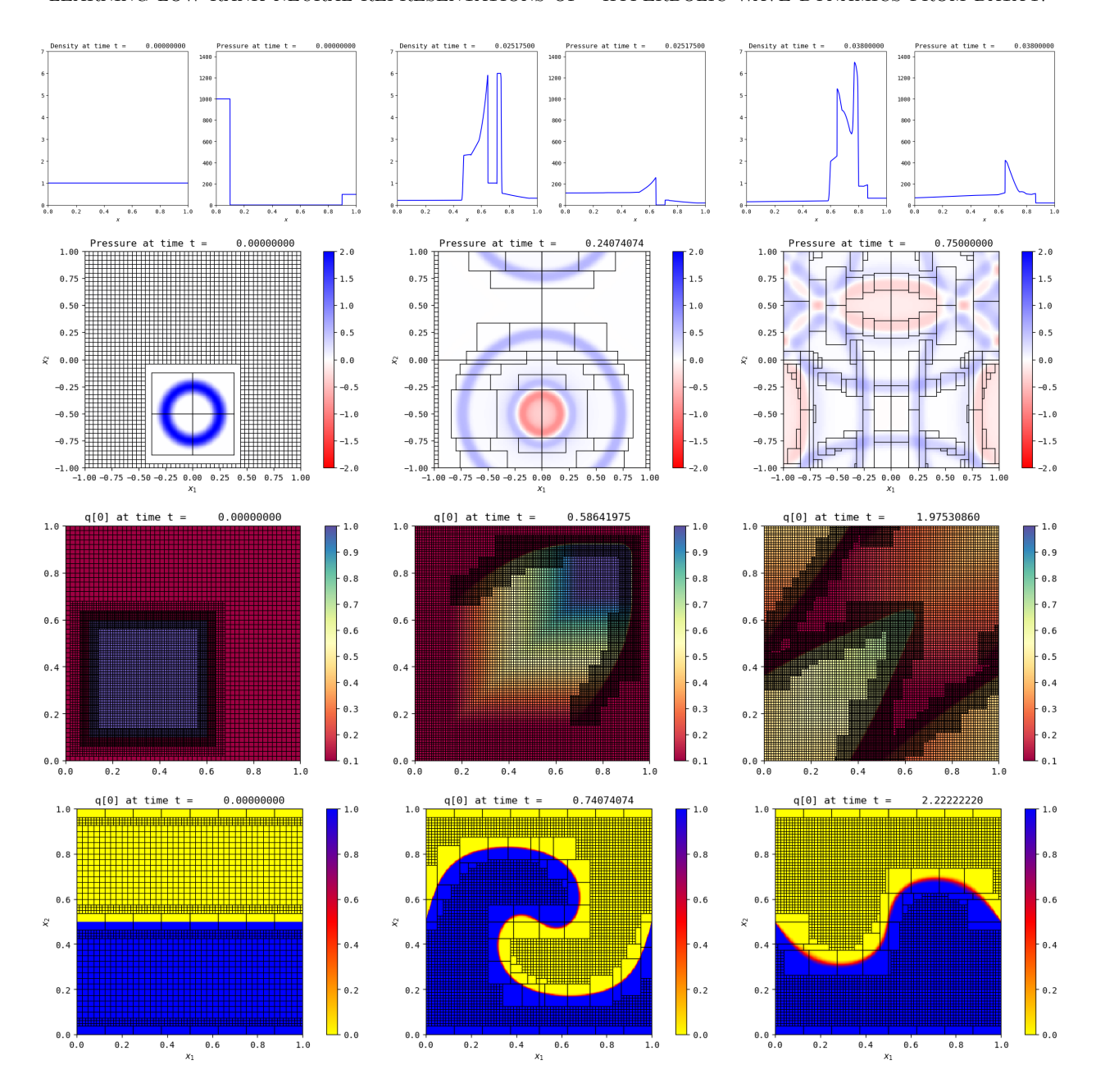


FIGURE 3. Plots of training data from the 1d Euler example (first row), 2d acoustics (second row), 2d Burgers (third row), and 2d advection (fourth row). For the 2d examples, AMR (Adaptive Mesh Refinement) data were used, where the finest-grid values at each spatial location were extracted as training data. The grid edges indicate the boundaries of AMR patches [7]. All data were generated using the Clawpack software package [28].

The orthogonality regularization tends to stabilize only after the loss function switches from MSE to  $\ell_1$ . This suggests that the training process prioritizes enforcing sparsity in the coefficient variables before gradually promoting orthogonality in the basis vectors.

4.3.2. Comparison with vanilla SIREN. The trained LRNR result is compared against that of the hypernetwork-SIREN approach trained with the MSE loss. In Fig. 6, we plot the  $\ell_2$  misfit (the

square root of the MSE loss) to enable visual comparison with the  $\ell_1$  misfit obtained from LRNR training in the later epochs. The  $\ell_2$  loss for SIREN decreases initially but diverges abruptly after approximately 100K epochs. We display the trained SIREN output prior to this divergence and compare it with the LRNR representation in Fig. 4. The SIREN result remains oscillatory despite a similar number of training iterations.

For the hypernetwork-SIREN, we use a SIREN INR with width 512 and depth 5. A smaller width of 256 failed to achieve comparable loss levels. The accompanying hypernetwork has width 256 and depth 5, with scalar modulation parameters also tuned. Recall that the hypernetwork outputs the full set of weights and biases for the SIREN network. Although the hypernetwork has width 256, implying that its output lies in a 256-dimensional space, this low-rank structure is not preserved once the outputs are reshaped into the appropriate weight and bias matrices. In particular, singular value decomposition (SVD) of the resulting  $512 \times 512$  weight matrices shows no significant decay in singular values.

Neural implicit flow models exhibit a similar architecture to the hypernetwork-SIREN [83], where the hypernetwork output is enforced to be low-rank. However, these models reshape the hypernetwork outputs into INR weights and biases in a similar manner, meaning that the resulting matrices do not necessarily possess a low-rank structure. In contrast, the LRNR architecture imposes an explicit low-rank matrix structure, resulting in a trained model whose weight matrices are structurally distinct from both hypernetwork-SIREN and neural implicit flow.

It is important to note, however, that the presented results are not intended as a direct comparison with those of SIREN. The trained LRNR models exhibit structural features and properties that are absent in SIRENs. Even if a SIREN can be trained to achieve similar reconstruction accuracy, the low-dimensional structures intrinsic to LRNR, which will be discussed in the following sections, would still be lacking. Conversely, it is certainly possible to incorporate key features of the SIREN architecture into LRNRs, for instance by employing sine activation functions or introducing modulation parameters. Whether the well-known advantages of SIREN architectures carry over to the LRNR setting remains an open research question, which we do not explore in this work.

4.3.3. Hyperparameters. The hyperparameters used in our experiments are summarized in Tab. 1. Hyperparameter selection was more consistent across the 2d examples, all of which employed adaptive mesh refinement (AMR) data. For the 1d case, which used a uniform spatial grid, mollification of the data was necessary. The misfit switch threshold was set to  $5 \times 10^{-4}$  for the 1d Euler example and  $5 \times 10^{-3}$  for the 2d examples. The initial learning rate was set to  $10^{-3}$ , with a ReduceLROnPlateau scheduler applied using a decay factor of 0.98, patience of 10 epochs, and a threshold of  $10^{-3}$ .

The results were particularly sensitive to the values of  $\lambda_{\text{sparse}}$  and  $\gamma$ , whereas  $\lambda_{\text{ortho}}$  had a relatively minor impact. Values of  $\lambda_{\text{ortho}}$  around  $10^{-2}$  produced acceptable results across all examples. In addition to reducing memory requirements, the use of AMR data in the 2d cases also eliminated the need for mollification.

### 5. Hypermodes and low-rank tensor representation

A remarkable property of neural network-based autoencoders is that even when given complicated spatial data, the dynamics in the latent variables can be very smooth [66, 42]. In the d'Alembert solution for the 1d wave equation (1.1), we have already seen that the time-dependent coefficients  $\pm ct$  were linear in time t (1.2), regardless of the regularity of the wave profiles f and g.

For LRNRs, this phenomenon is also observed in other theoretical constructions (Thms. 3.2-3.3), even for entropy solutions involving nonlinear shock interactions (Thm. 3.4; [96]). A particularly notable feature of these constructions is that the coefficient variables exhibit linear (or constant) dependence on time, despite the presence of discontinuous spatial behavior in the solution.

	M	r	L	$M_{ m hyper}$	$L_{\mathrm{hyper}}$	batch	$\lambda_{ m sparse}$	$\lambda_{ m ortho}$	$\gamma$	grid
1d Euler	1200	150	5	25	4	16	3.65e-18	7.76e-3	1.0005	unif
2d acoustics	2000	190	4	10	3	1	2.35e-08	1.00e-2	1.0500	adapt
2d Burgers	2000	170	4	10	3	1	2.71e-11	1.00e-2	1.0500	adapt
2d advection	2000	180	4	10	3	1	3.48e-10	1.00e-2	1.0650	adapt

TABLE 1. Tuned hyperparameters. M, r, and L denote the width, rank, and depth of the LRNR, respectively.  $M_{\rm hyper}$  and  $L_{\rm hyper}$  refer to the width and depth of the hypernetwork. "Batch" refers to the batch size.  $\lambda_{\rm sparse}$  is the regularization parameter for the sparsity-promoting regularizer, while  $\lambda_{\rm ortho}$  is the regularization parameter for the orthogonality regularization term.  $\gamma$  controls the coefficient value decay. The last column indicates the type of input data used for each example.

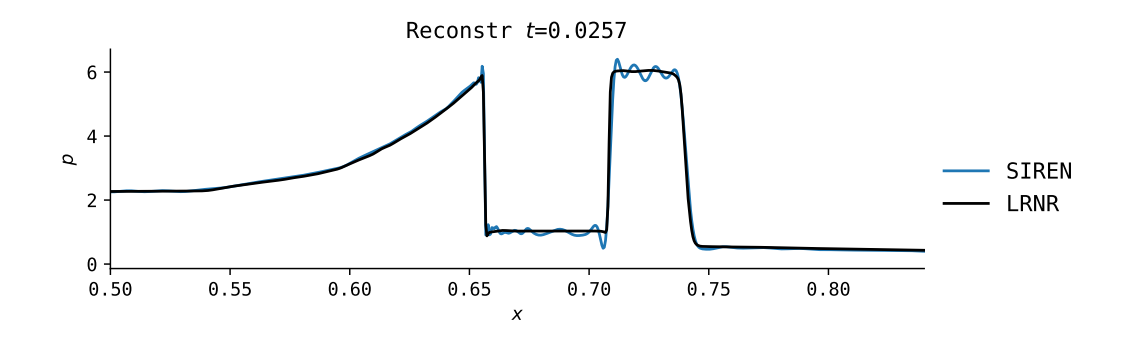


FIGURE 4. Comparison of reconstructions between SIREN and LRNR. Oscillations persist in the SIREN model trained with MSE loss, whereas the LRNR reconstruction exhibits damped oscillations and sharper jump discontinuities.

This observation leads us to the question of whether the trained LRNRs using the hypernetwork approach exhibit similar time regularity. In Fig. 7, we plot the evolution of the coefficient outputs from the hypernetwork for the 1d Euler equations, and we observe that: (1) Many components of the coefficients remain close to zero throughout, suggesting a time-uniform low-rank structure; and (2) the coefficients evolve smoothly over time and appear approximately linear.

Motivated by these observations, we investigate two types of reductions: (1) truncating coefficients by discarding uniformly small entries, and (2) exploiting temporal regularity. The first truncation can be applied independently to each weight and bias component. We denote by  $r_1^{\ell}$  the truncated rank of the weight matrix  $\mathbf{W}^{\ell}$ , and by  $r_2^{\ell}$  the truncated rank of the bias vector  $\mathbf{b}^{\ell}$ . The resulting truncated ranks are reported in Tab. 2. The reduction is substantial, indicating that the sparsity-promoting regularizer was effective in inducing coefficient decay. Beyond this straightforward reduction, however, the coefficient evolution plots in Fig. 7 reveal another possibility: a reduction in the dynamics of the full coefficient vector as a whole. We explore this aspect in the following section.

5.1. Hypermodes and low-rank tensor decomposition. We begin by noting that  $f_{\text{hyper}}$  is relatively small (Tab. 1), so it is feasible to explicitly identify a low-dimensional linear subspace of its output range. To this end, we adopt a standard proper orthogonal decomposition (POD) approach [9]. Sampling  $f_{\text{hyper}}$  at N discrete time points, we form a snapshot matrix with the outputs of  $f_{\text{hyper}}$  as columns:

(5.1) 
$$\mathbf{S}_{\text{data}} = \left[ f_{\text{hyper}}(t_1) \mid f_{\text{hyper}}(t_2) \mid \dots \mid f_{\text{hyper}}(t_{N-1}) \mid f_{\text{hyper}}(t_N) \right].$$

#### Woodward-Colella problem

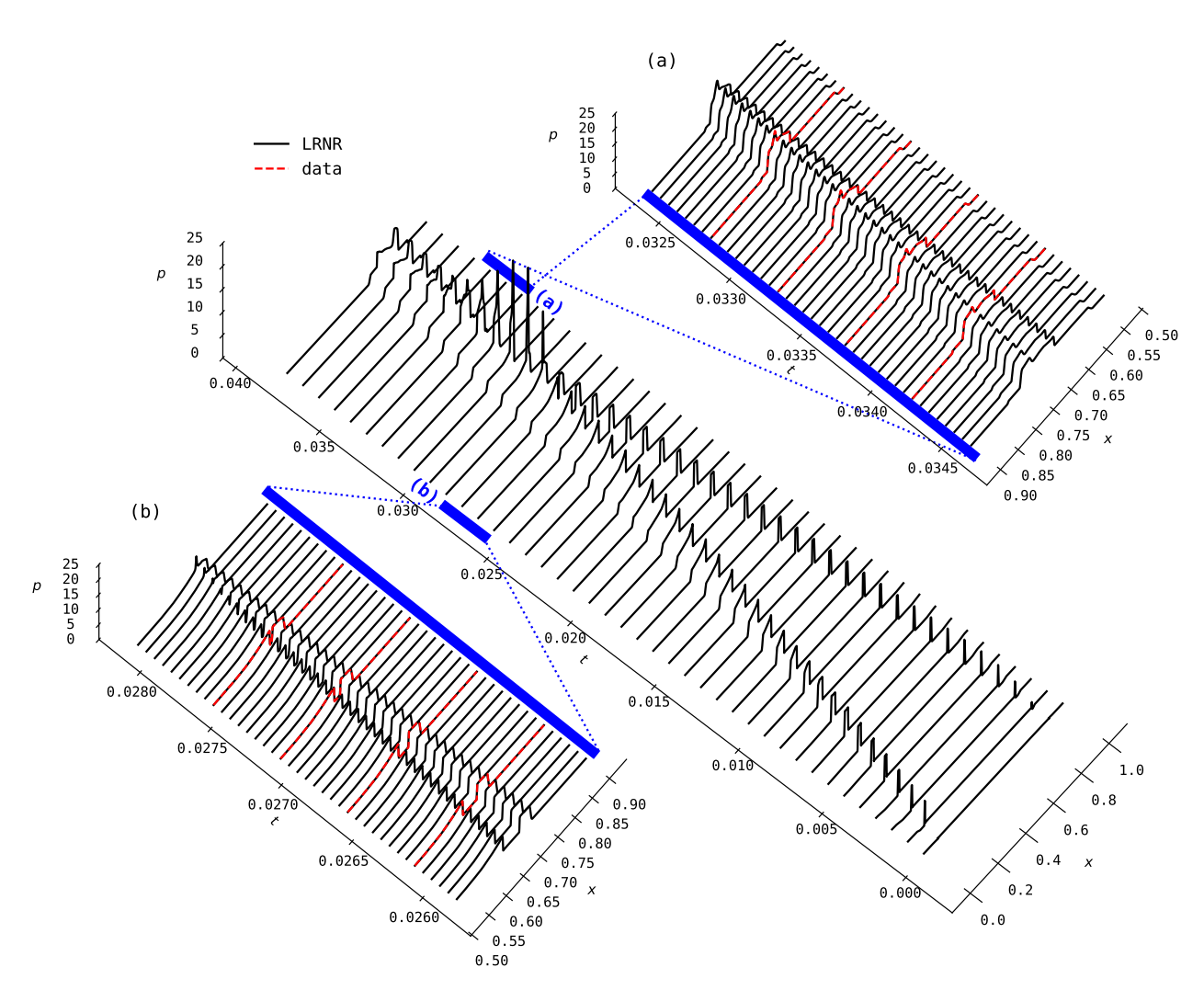


FIGURE 5. LRNR reconstruction of the solution to the 1d compressible Euler equations with periodic boundary conditions (Woodward-Colella shock problem [111, 110, 67]). (a,b) Zoom-in plots highlight the learned representation at interpolated times,  $u(\cdot; f_{\text{hyper}}(t))$ . In (a), the rarefaction waves and shocks that emerge after the shock collision are individually transported with high accuracy. In (b), the sharp peak formed at the shock merger is correctly placed and closely mimics the behavior of the finite volume solution, despite the fact that the precise timing of the collision must be inferred from data.

We then compute the SVD of this matrix:

$$\mathbf{S}_{\text{data}} = \mathbf{\Phi} \mathbf{D} \mathbf{\Psi}^{\top}.$$

Here, the left-singular vectors  $\phi_i$ , which form the columns of  $\Phi$ , provide a basis for the full space of coefficient vectors spanning both weights and biases. We refer to these vectors  $\phi_i$  as hypermodes. For the j-th left singular vector  $\phi_j$  in (5.2), we denote the entries corresponding to the coefficients  $s_{1,j}^{\ell}$  and  $s_{2,j}^{\ell}$  as  $\phi_{1,ij}^{\ell}$  and  $\phi_{2,ij}^{\ell}$ , respectively. After truncating the negligible singular values, the

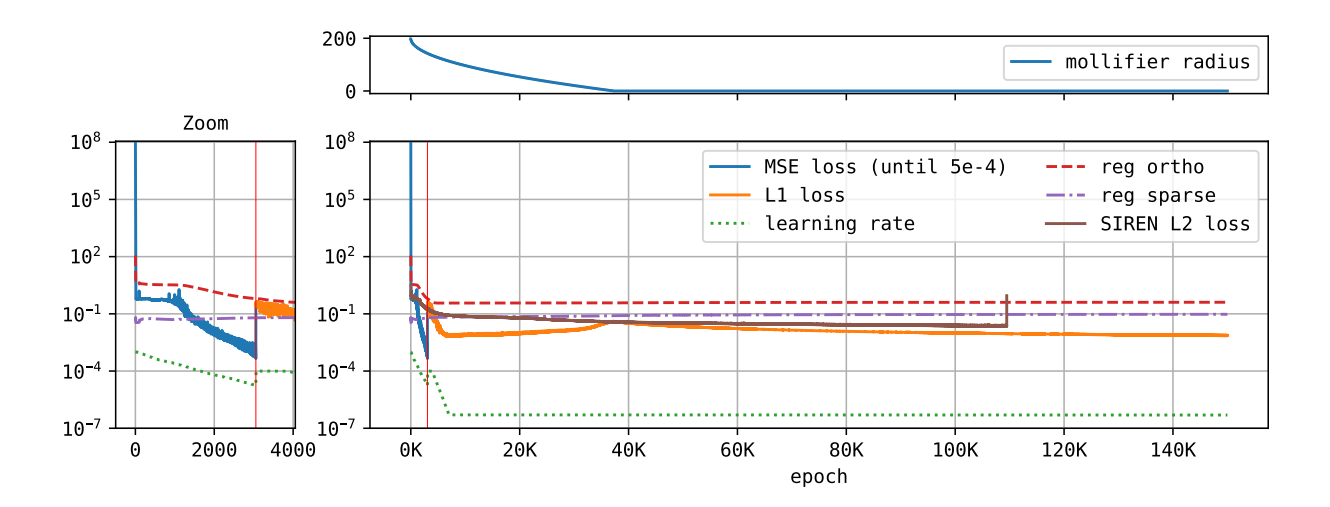


FIGURE 6. Scaled MSE loss is used until a threshold of 5e-4 is reached, and then the misfit loss is switched to the  $L_1$  loss. Mollifier radius is set to decrease linearly according to the schedule given above. A zoom-in near the epochs when the misfit function is switched is shown to the left. Orthogonality and sparsity regularizer terms stay relatively flat throughout training, except that orthogonality is not strongly enforced until around epoch 5K. As the mollifier radius is relaxed, the loss increases due to an increase in the misfit, however, once the radius is zero, a slow but steady decrease in the  $\ell_1$  loss is observed. Spurious oscillatory behavior near the shock is removed during this period of training.

weights and biases can be expressed as:

(5.3) 
$$\mathbf{W}^{\ell}(\mathbf{c}) = \sum_{i=1}^{r_1^{\ell}} \sum_{j=1}^{\bar{r}} c_j \phi_{1,ij}^{\ell} \otimes \mathbf{u}_i^{\ell} \otimes \mathbf{v}_i^{\ell}, \qquad \mathbf{b}^{\ell}(\mathbf{c}) = \sum_{j=1}^{r_2^{\ell}} c_j \phi_{2,ij}^{\ell} \mathbf{b}_i^{\ell}, \qquad \ell = 1, 2, \dots, L.$$

The third-order tensor term arises naturally in this formulation,

(5.4) 
$$\phi_{1,i}^{\ell} \otimes \mathbf{u}_{i}^{\ell} \otimes \mathbf{v}_{i}^{\ell}, \quad i = 1, \dots, r_{1}^{\ell},$$

and the sum

(5.5) 
$$\sum_{i=1}^{r_1^{\ell}} c_j \phi_{1,ij}^{\ell} \otimes \mathbf{u}_i^{\ell} \otimes \mathbf{v}_i^{\ell}$$

constitutes a rank- $r_1^{\ell}$  tensor decomposition.

Using the truncated left singular matrix  $\tilde{\Phi}$  from the POD decomposition, we define a reduced hypernetwork output by projecting onto the low-dimensional subspace:

(5.6) 
$$\hat{f}_{hyper}(t) = \hat{\boldsymbol{\Phi}} \hat{\boldsymbol{\Phi}}^{\top} f_{hyper}(t).$$

In our experiments, we observe a rapid decay in the singular values (a rapid decay in the diagonal values of  $\mathbf{D}$ ). They are shown in Fig. 8. We know that  $\mathbf{\Phi}$  is necessarily low rank upon truncation, since the rank of  $S_{\text{data}}$  is at most the width of the hypernetwork. The time-dynamics is described by the basis  $\Psi$ , and one sees that they are very smooth. The smooth dynamics can also be approximated by polynomials; degrees up to 30 suffice to approximate all components to machine precision

	$\mid r \mid$	$r_{1}^{1}$	$r_{1}^{2}$	$r_{1}^{3}$	$r_1^4$	$r_1^5$	$r_{2}^{1}$	$r_{2}^{2}$	$r_{2}^{3}$	$r_{2}^{4}$	$r_2^5$	$ar{r}$
1d Euler	150	38	28	94	147	35	71	58	76	67	113	5
2d acoustics	190	64	125	116	14		63	85	74	3		23
2d Burgers	170	14	32	113	4		11	14	16	7		38
2d advection	180	85	160	158	5		29	37	20	9		26

TABLE 2. Truncated coefficient parameters and number of significant hypermodes (5.2). The truncation threshold was set to  $5 \times 10^{-5}$  after normalizing so that the largest coefficient value equals 1.

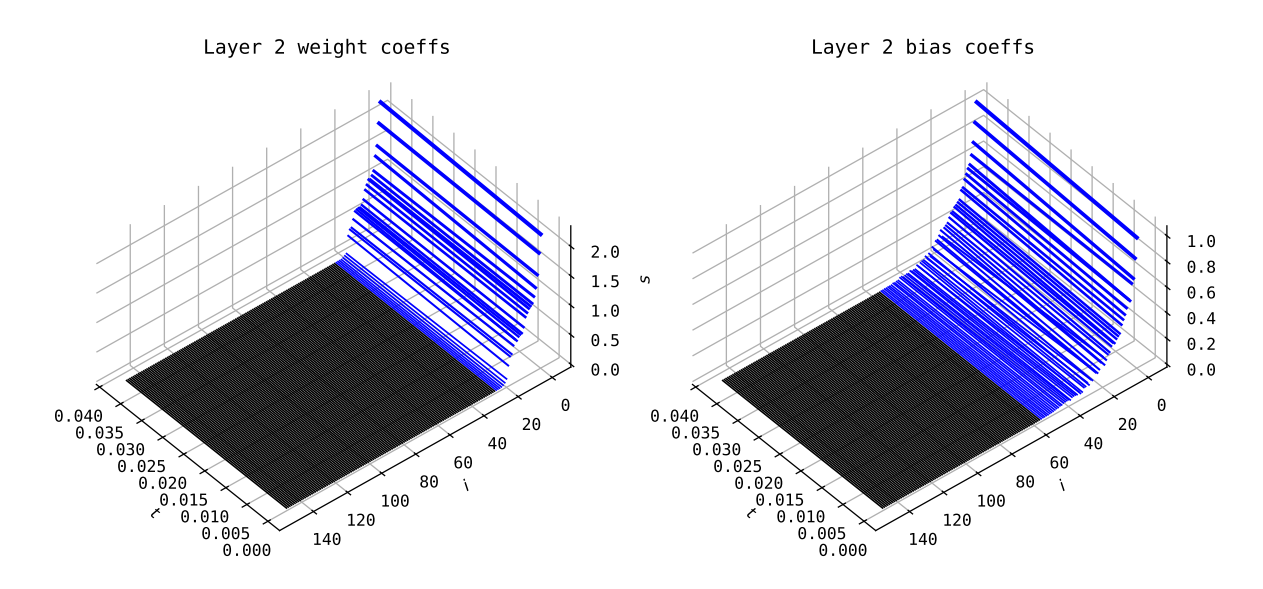


FIGURE 7. A plot of the coefficients in layer  $\ell=2$  for the weights (left) and the bias (right). Many of the coefficients are zero, showing that truncation of certain terms in the rank-1 expansion (2.6) can reduce the number of coefficients. The evolution appears smooth and in most cases looks like straight lines, making them representable by a few basis functions themselves, leading to the hypermodes (5.2).

5.2. **Hypermode tangents.** The tensor decomposition (5.3) yields a new set of coordinates  $\mathbf{c} = (c_i)_{i=1}^{\bar{r}}$ , which we refer to as hypermode coordinates. A key distinction from the low-rank structure built into the LRNR architecture is that this tensor decomposition introduces coupling across different layers. In contrast, the low-rank weight matrices in the LRNR architecture (2.6) enforce low-rank structure independently within each layer, without inter-layer dependencies. This is reminiscent of the cross-layer coupling in standard hypernetwork formulation.

One can interpret the time dynamics as a curve embedded in the new coordinate system, represented by the dynamic hypermode coordinates  $\mathbf{c}(t) = (c_i(t))_{i=1}^{\bar{r}}$ . At each time t, we can examine the effect of perturbing this curve along the hypermode directions  $\phi_i$  and analyze how the LRNR responds to these perturbations:

(5.7) 
$$u(\bullet; \mathbf{s} + \delta \mathbf{s}_i), \text{ where } \delta \mathbf{s}_i = \mathbf{\Phi} \mathbf{c}(t) + \eta_i \phi_i, \quad \eta_i \ll 1,$$

where  $\Phi$  is the left-singular-vector matrix computed from (5.2), and  $\phi_i$  is the *i*-th hypermode. The scalar  $\eta_i$  is selected to ensure that each perturbation produces a visually comparable effect in the output. These variations can be viewed as dominant modes in the nonlinearly transformed coefficient space.

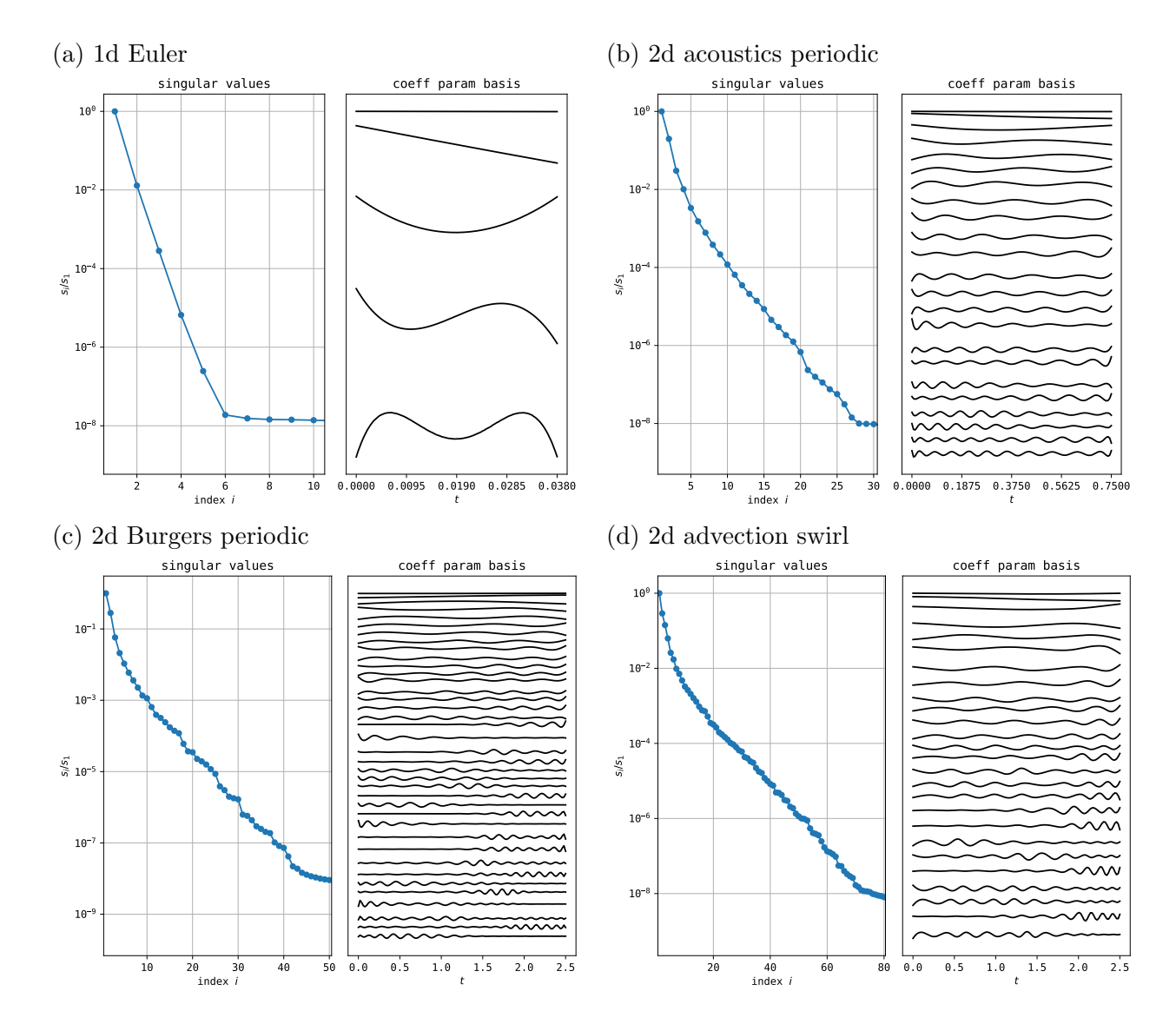


FIGURE 8. Singular values of the coefficient snapshots over time for the given hyperbolic examples. The corresponding right-singular vectors, which form a shared temporal basis for the coefficient dynamics, are shown on the right. These temporal modes are highly regular.

5.2.1. 1d Compressible Euler. The perturbations along dominant hypermodes are shown for the 1d Euler equation in Fig. 9. Notably, the first two modes govern the evolution of key features in the pressure profile. Perturbing along the first mode shifts the two shock locations and slightly increases the separation between the peaks. In contrast, the second mode draws the peaks closer together. After the collision, the two modes influence the placement of transient regions: for example, the first mode significantly shifts the left-most inclined slope, whereas the second mode leaves it largely unchanged. Overall, the first mode tends to shift the entire profile to the right, while the second mode widens the central region.

Focusing on the time t = 0.0285, after the two shocks have merged into a single large peak, perturbations in the hypermodes induce physically plausible variations in the shape of the peak. The first mode shifts the peak and its adjacent slopes to the right. The second mode increases the peak height while narrowing its width, and depresses the left-side slope, and pulls it toward

the peak. The third mode narrows and lowers the peak while steepening the left slope, leaving the right slope nearly unchanged. The fourth mode raises and broadens the peak, steepens the right slope, and introduces a discontinuity in the otherwise smooth descent. The fifth mode keeps both left and right slopes intact but shifts the peak significantly to the left.

5.2.2. 2d Acoustics with periodic boundary conditions. The perturbations for the 2d acoustics equation are shown in Fig. 10. Perturbations along the second hypermode are plotted using dashed lines. This mode appears to induce a time-advancing effect in the solution. For example, at t = 0.04, the perturbation anticipates the incoming wave from the upper boundary. At t = 0.38, it emphasizes the formation of two narrow peaks near the line  $x_2 = 0.75$ , while largely ignoring the development of the broader, oblong peak. At later times, the perturbation continues to act primarily on the narrow peaks and leaves the flatter, right-angle-aligned wavefronts, those oriented along the axes from the origin, mostly unchanged.

Fig. 11 shows the effect of perturbations along different hypermodes at a fixed time t=0.67. The first mode shifts the entire solution downward uniformly, indicating a global offset in amplitude. The second mode roughly corresponds to temporal evolution, as previously observed. The third mode primarily transports the connecting contours between the peaks. The fourth mode significantly depresses the central region while preserving the corner peaks. The fifth mode widens the peaks slightly. The sixth mode introduces minor shifts in peak positions; for instance, the two upper peaks near  $x_2=0.50$  move slightly closer to the center.

5.2.3. 2d Burgers with periodic boundary conditions. The hypermode perturbations for the 2d Burgers equation are shown in Fig. 12. As in the 2d acoustics case, perturbation along the second hypermode appears to approximate a forward time-evolved solution. The shock at the upper-right tip becomes sharper, the rarefaction fan shifts backward, and the incoming profiles at the upper-left and lower-right corners move inward.

Fig. 13 shows the effect of different hypermode perturbations at time t = 1.50. The first mode primarily affects the rarefaction fans, moving the sloped regions backward while leaving the shocks mostly unchanged. The second mode corresponds roughly to forward time evolution. The third mode adjusts the central slope while preserving most of the contour structure. The fourth mode modifies the slope and shock contours along the diagonal from the lower-left to upper-right, without significantly affecting the intruding jumps from the upper-left and lower-right corners. The fifth mode alters the shape of the shock tip near  $(x_1, x_2) = (0.4, 0.4)$  and moves the slanted intruding profiles downward. In contrast, the sixth mode also modifies the shock tip but shifts the intruding profiles upward.

5.2.4. 2d Advection with variable speed. The hypermode perturbations for the 2d advection equation are shown in Fig. 14. Perturbation along the second hypermode (similar to the acoustics 2d case) appears to approximate a forward time-evolved solution, generally twisting the curved interface in the advection direction. At time t=1.80, it even predicts the return to the initial condition, where the interface lies along the straight line  $x_2=0.5$ .

Fig. 15 shows the effect of different hypermode perturbations at time t = 2.40. The first mode corresponds to a slight up-down shift of the contours. The second mode again resembles forward time evolution. The third mode primarily adjusts the vertical heights of the contours, with a minor twist in the up-down direction. The fourth mode modifies the shape of the twisting interface, particularly the portion in the upper-left region of the domain. The fifth mode similarly adjusts the interface, this time focusing on the lower-right region. The sixth mode slightly forward-evolves the solution while also altering the curve's vertical position, pushing the upper-left portion downward and the lower-right portion slightly upward.

### Coefficient tangents

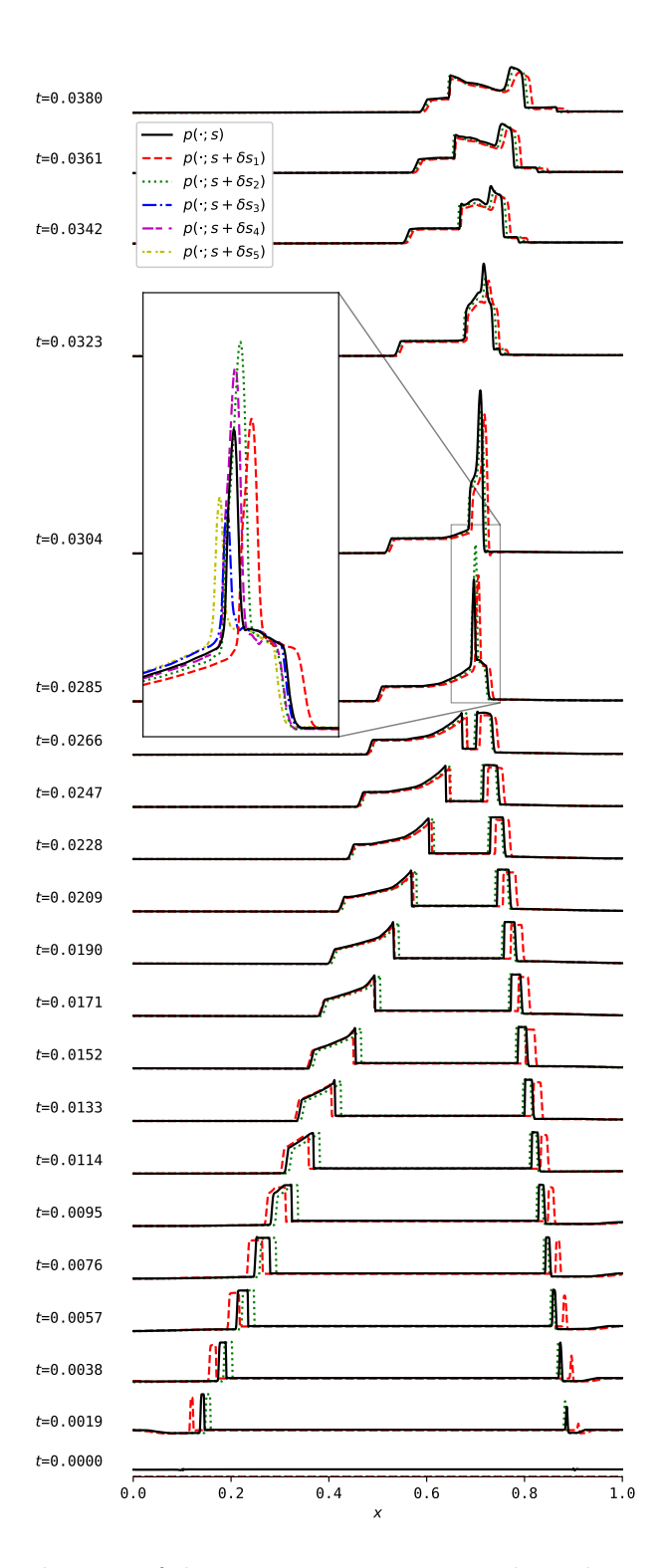


FIGURE 9. Perturbations of the LRNR reconstruction along the coefficient tangents defined by the hypermodes (5.2). Shown are the effects of the first two hypermode perturbations, including a zoom-in view near time t=0.0285, shortly after the shock collision. Each hypermode reveals plausible directions of evolution for the solution at different times.

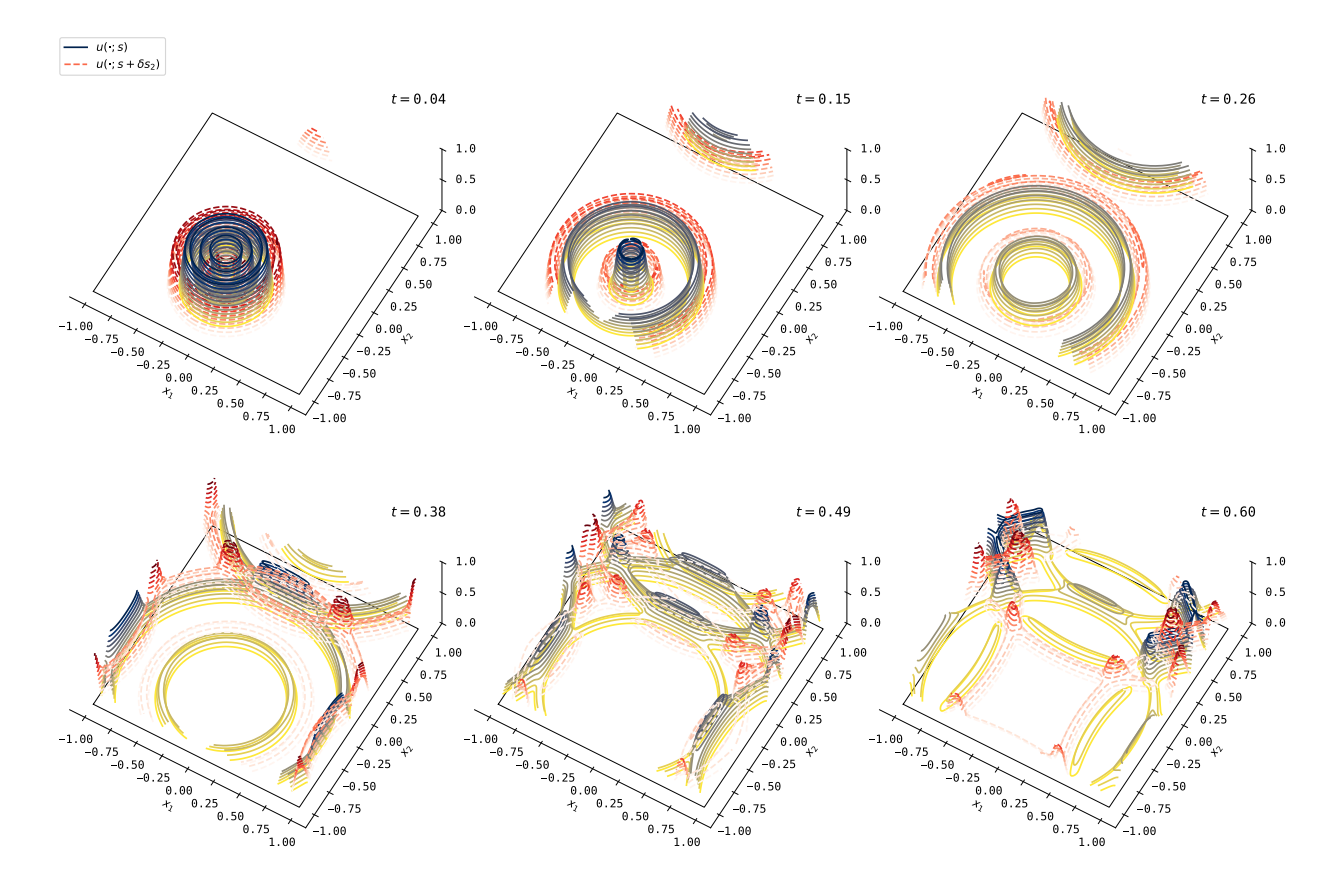


FIGURE 10. 2d acoustics example: LRNR reconstruction (solid contours) and the effect of perturbing the coefficients along a selected hypermode direction (dashed contours) at various time instances.

5.3. **Hypermode extrapolation.** The coefficient tangent directions given by the hypermodes (5.7) appear to capture dominant directions that the solution dynamics tends to follow. Interestingly, however, these hypermodes continue to produce salient features even when the coefficient vectors are perturbed significantly beyond their training-time trajectories. As the perturbation magnitude increases, the coefficients move outside the range seen during training, resulting in wave profiles that were never observed in the actual solution trajectory.

This behavior can be interpreted as a form of coefficient extrapolation in the hypermode directions, extending beyond the local tangents near the solution trajectory. Specifically, we consider traversing further along the hypermode perturbation directions (5.2), as given by:

(5.8) 
$$u(\bullet; \mathbf{s} + \delta \mathbf{s}_i), \text{ where } \delta \mathbf{s}_i = \mathbf{\Phi} \mathbf{c}(t) + \eta_i \phi_i \mathbf{c}'_i(t), \quad \eta_i \sim 1.$$

Unlike many convolutional autoencoder models, where large extrapolations from training data often yield outputs lacking coherent structure, these extrapolations in the LRNR setting still produce reconstructions that retain physically meaningful features.

We illustrate that, for LRNRs, extrapolation remains meaningful even far beyond the local tangent space. This is demonstrated in the 1d Euler example shown in Fig. 16. Extrapolation along the first hypermode largely translates the profile to the right while simultaneously smoothing the sharp features. Along the second hypermode, the peak height decreases, and the previously gradual slope on the left is sharpened into a jump discontinuity. The third mode produces a profile reminiscent of an earlier, pre-collision state, removing the central peak and splitting the wave into two distinct components. The fourth hypermode initially sharpens and narrows the peak, but also

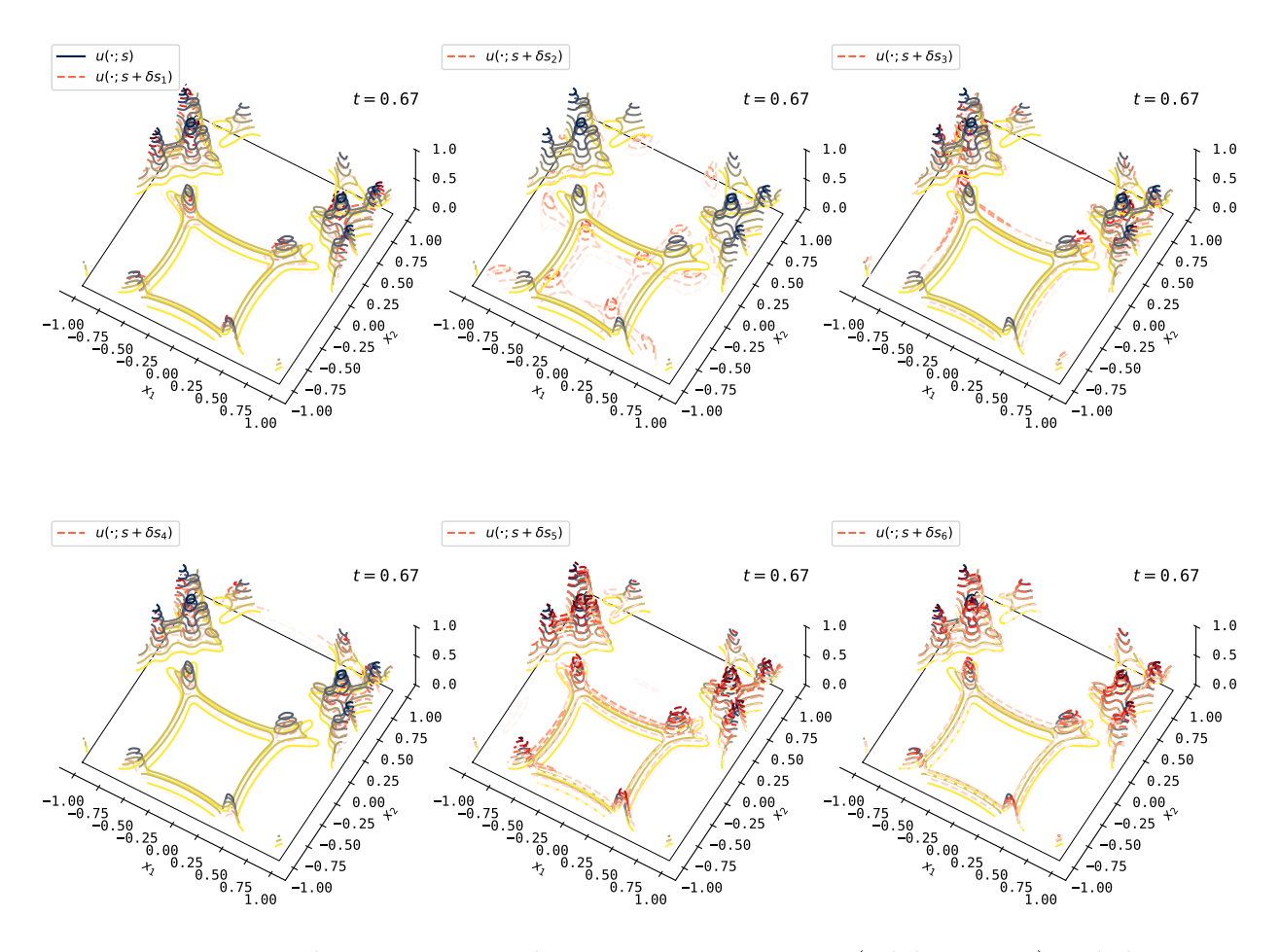


FIGURE 11. 2d acoustics example: LRNR reconstruction (solid contours) and the effect of coefficient perturbations along various hypermode directions (dashed contours) at a fixed time.

introduces a kink along the left slope and transforms the right side into a nearly linear descent. Extrapolation along the fifth mode yields a similar split behavior to the third mode, but with the resulting profile shifted to the right and the left peak significantly smaller than the right.

These extrapolated profiles bear little resemblance to any solution data on which the LRNR was trained, yet they retain coherent structures that appear physically plausible. Notably, even when deviating significantly from the trajectory  $t \mapsto \mathbf{c}(t)$  defined by the hypernetwork outputs, the resulting profiles do not exhibit random or noisy artifacts.

# 6. FASTLRNR AND EFFICIENT EVALUATION

A key limitation of INRs in practical applications is their slow inference speed. For example, in SIREN hypernetworks, the INR typically consists of fully connected layers with widths exceeding  $2^9 = 512$ . Even with such moderately sized networks, evaluating the output at a single point involves computations that scale with network width, which becomes prohibitively expensive in performance-critical applications such as real-time rendering, as discussed in well-known works [79, 57]. We highlight another advantage of the LRNR architecture: its low-rank structure enables accelerated evaluation and backpropagation [26]. Here, we focus on the forward evaluation (inference) at a single spatial point, which is the fundamental operation underlying reconstruction.

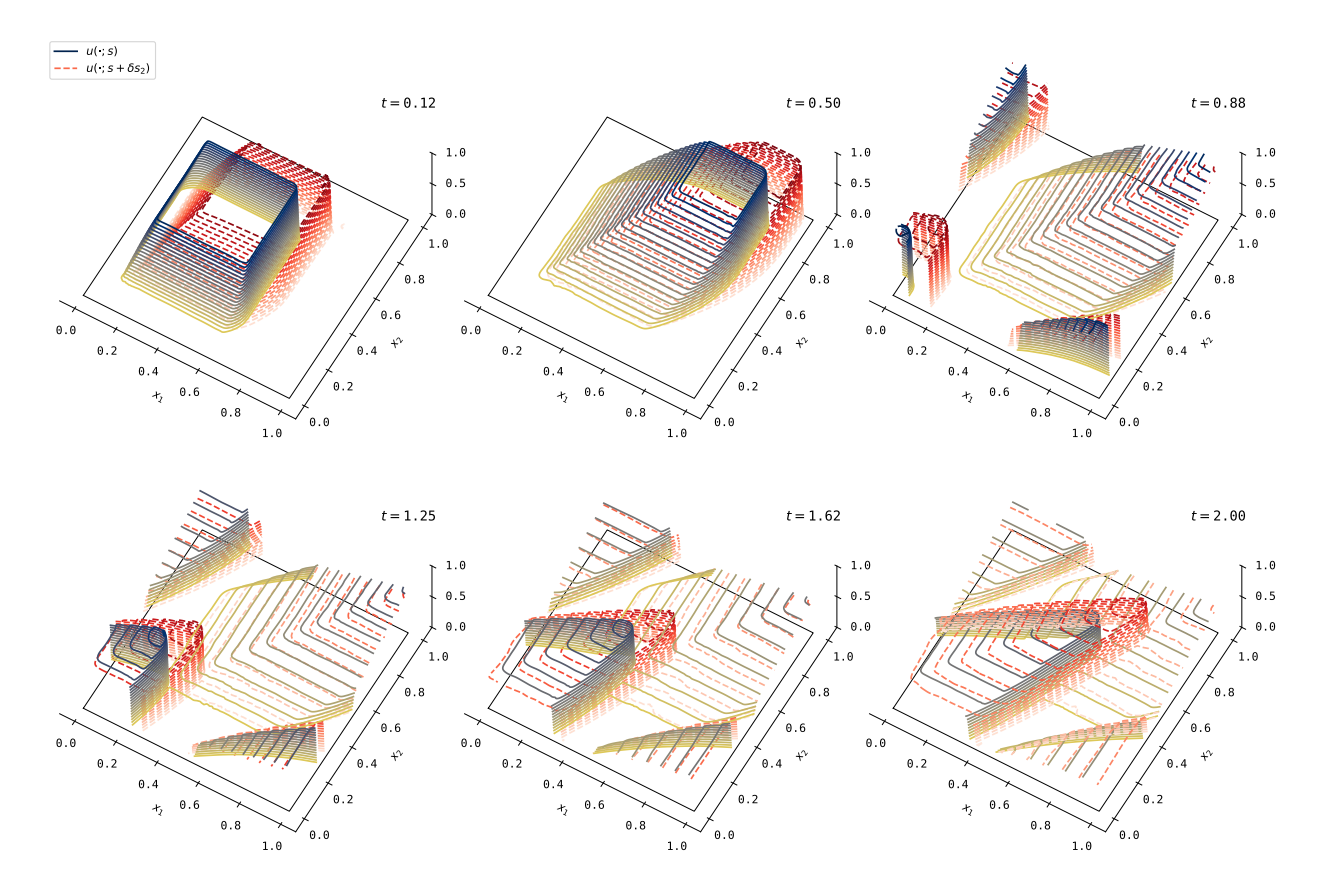


FIGURE 12. 2d Burgers equation example: LRNR reconstruction (solid contours) and the effect of coefficient perturbations along a hypermode direction (dashed contours) at various times.

6.1. **FastLRNR construction.** A distinguishing feature of LRNRs is that at each layer, the output from the affine mapping

(6.1) 
$$\mathbf{y}^{\ell} = \mathbf{W}^{\ell} \mathbf{z}^{\ell-1} + \mathbf{b}^{\ell}$$

$$= \mathbf{U}^{\ell} \operatorname{diag}(\mathbf{s}_{1}^{\ell}) \mathbf{V}^{\ell \top} \mathbf{z}^{\ell-1} + \mathbf{B}^{\ell} \mathbf{s}_{2}^{\ell}$$

$$= \begin{bmatrix} \mathbf{U}^{\ell} & \mathbf{B}^{\ell} \end{bmatrix} \begin{bmatrix} \boldsymbol{\zeta}^{\ell} \\ \mathbf{s}_{2}^{\ell} \end{bmatrix}, \qquad (\boldsymbol{\zeta}^{\ell} := \operatorname{diag}(\mathbf{s}_{1}^{\ell}) \mathbf{V}^{\ell \top} \mathbf{z}^{\ell-1})$$

has rank at most  $r_1^{\ell} + r_2^{\ell}$ . When a scalar nonlinearity is applied to this output,

(6.2) 
$$\mathbf{z}^{\ell} = \sigma \left( \begin{bmatrix} \mathbf{U}^{\ell} & \mathbf{B}^{\ell} \end{bmatrix} \begin{bmatrix} \boldsymbol{\zeta}^{\ell} \\ \mathbf{s}_{2}^{\ell} \end{bmatrix} \right),$$

the result  $\mathbf{z}^{\ell}$  may also lie in a low-rank linear subspace, provided the nonlinearity  $\sigma$  is smooth. This property, often referred to as *affine decomposition*, has long been leveraged in classical reduced-order models [50], where one writes

(6.3) 
$$\mathbf{z}^{\ell} = \mathbf{\Xi}^{\ell} \mathbf{q}^{\ell}, \qquad \mathbf{\Xi}^{\ell} \in \mathbb{R}^{M_{\ell} \times \hat{r}^{\ell}}$$

for some  $\hat{r}^{\ell} \approx r_1^{\ell} + r_2^{\ell}$ . That is, the output  $\mathbf{z}^{\ell}$  lies approximately in the column space colspan( $\mathbf{\Xi}^{\ell}$ ) of dimension  $\hat{r}^{\ell}$ . Although the basis matrix  $\mathbf{\Xi}^{\ell}$  is not known a priori, it can be constructed empirically by sampling  $\mathbf{z}^{\ell}$  for different values of the spatial input  $\mathbf{x}$  or the coefficient vector  $\mathbf{s}$ .

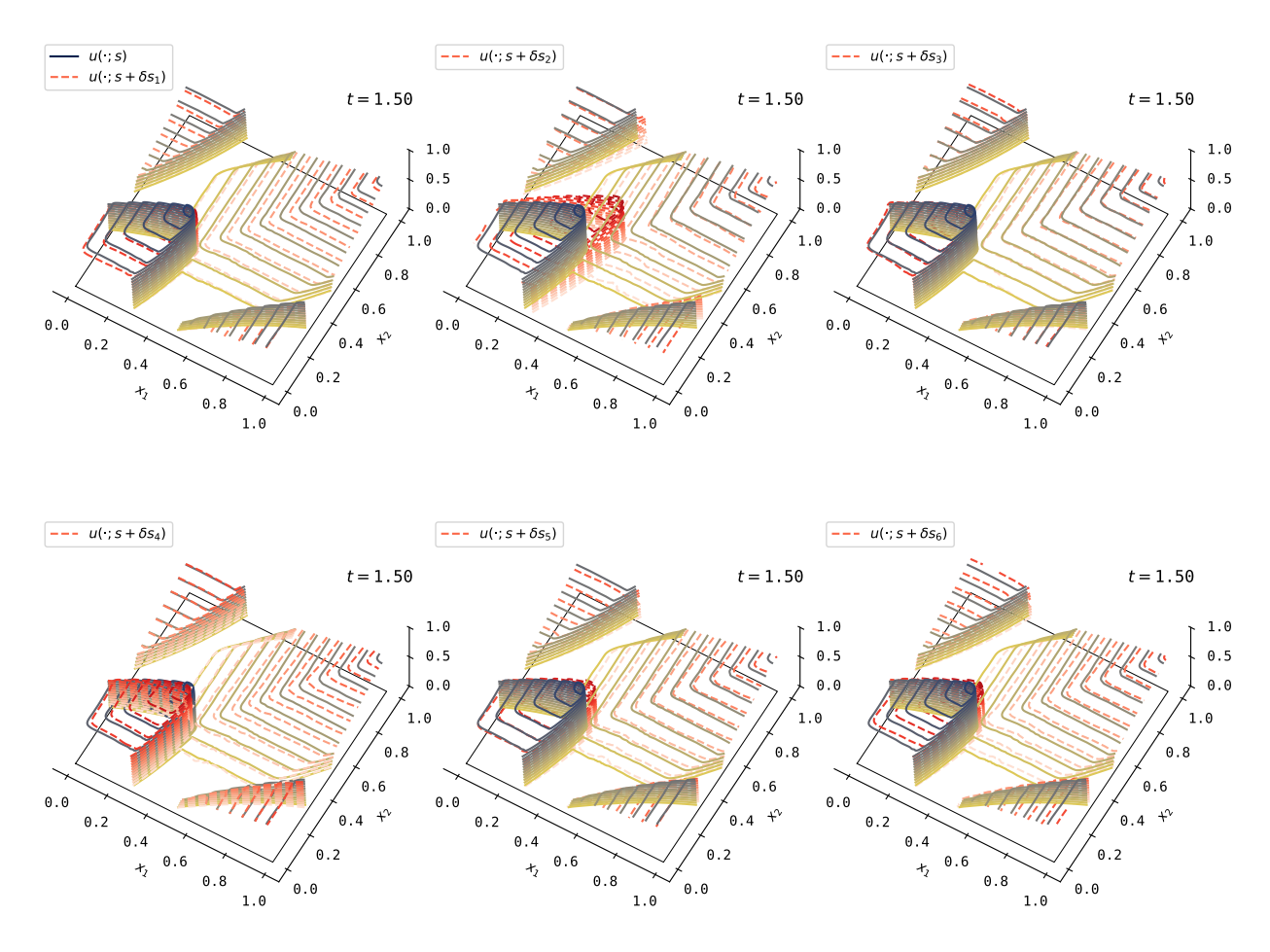


FIGURE 13. 2d Burgers equation example: LRNR reconstruction (solid contours) and the effect of coefficient perturbations along various hypermode directions (dashed contours) at a fixed time.

Although  $\mathbf{q}^{\ell}$  is also not known, it can be computed by solving a linear system. Since the system  $\mathbf{\Xi}^{\ell}\mathbf{q}^{\ell} = \mathbf{z}^{\ell}$  is typically overdetermined, we solve a reduced system by sampling a subset of the rows (assuming consistency):

(6.4) 
$$\mathbf{q}^{\ell} = \left(\mathbf{P}^{\ell \top} \mathbf{\Xi}^{\ell}\right)^{-1} \mathbf{P}^{\ell \top} \mathbf{z}^{\ell}$$

where  $\mathbf{P}^{\top}$  is a sampling matrix that selects (or truncates) rows from the product. This leads to the reduced reconstruction:

(6.5) 
$$\mathbf{z}^{\ell} = \mathbf{\Xi}^{\ell} \left( \mathbf{P}^{\ell \top} \mathbf{\Xi}^{\ell} \right)^{-1} \mathbf{P}^{\ell \top} \sigma(\mathbf{y}^{\ell}) = \mathbf{\Xi}^{\ell} \left( \mathbf{P}^{\ell \top} \mathbf{\Xi}^{\ell} \right)^{-1} \sigma(\mathbf{P}^{\ell \top} \mathbf{y}^{\ell}).$$

Taking into account the low-rank structure of the weight matrix in the next layer, we compute

(6.6) 
$$\mathbf{V}^{(\ell+1)\top}\mathbf{z}^{\ell} = \mathbf{V}^{(\ell+1)\top}\mathbf{\Xi}^{\ell} \left(\mathbf{P}^{\ell\top}\mathbf{\Xi}^{\ell}\right)^{-1} \sigma(\mathbf{P}^{\ell\top}\mathbf{y}^{\ell}).$$

In practice, the inverse is typically avoided and replaced with a linear solve. Notably, this formulation eliminates dependence on the full width  $M_{\ell}$  in the matrix products. Note that the matrix

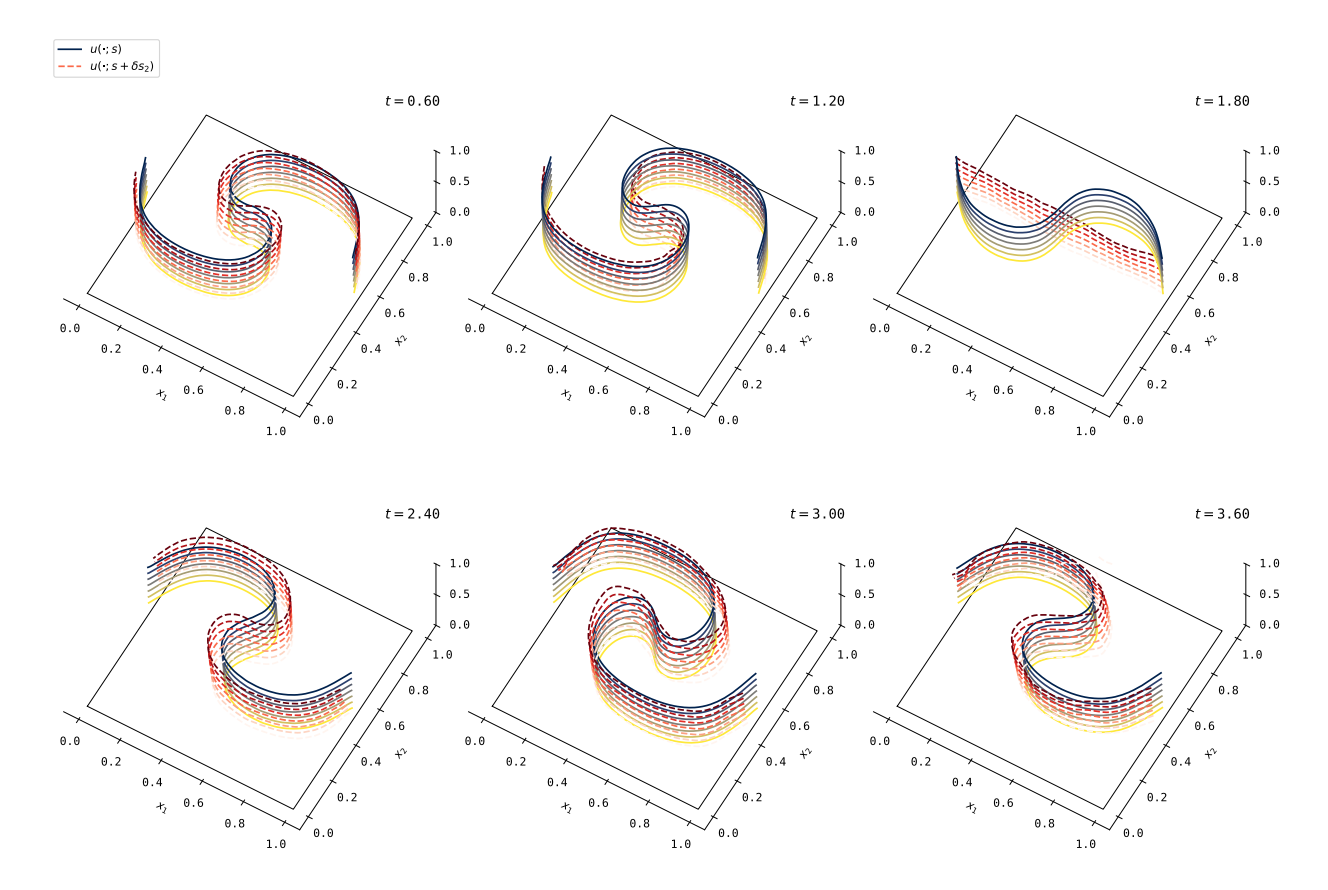


FIGURE 14. 2d advection equation example: LRNR reconstruction (solid contours) and the effect of coefficient perturbations along a hypermode direction (dashed contours) at various times.

dimensions are:

(6.7) 
$$\mathbf{V}^{(\ell+1)\top} \in \mathbb{R}^{r_1^{\ell+1} \times M_{\ell}}, \qquad \mathbf{\Xi}^{\ell} \in \mathbb{R}^{M_{\ell} \times \hat{r}^{\ell}}, \\ \mathbf{P}^{\ell\top} \in \mathbb{R}^{\hat{r}^{\ell} \times M_{\ell}}, \qquad \begin{bmatrix} \mathbf{U}^{\ell} & \mathbf{B}^{\ell} \end{bmatrix} \in \mathbb{R}^{M_{\ell} \times (r_1^{\ell} + r_2^{\ell})}.$$

We define compressed matrices:

(6.8) 
$$\hat{\mathbf{V}}^{(\ell+1)\top} := \mathbf{V}^{(\ell+1)\top} \mathbf{\Xi}^{\ell} \left( \mathbf{P}^{\ell\top} \mathbf{\Xi}^{\ell} \right)^{-1} \in \mathbb{R}^{r_1^{\ell+1} \times \hat{r}^{\ell}}, 
\hat{\mathbf{U}}^{\ell} := \mathbf{P}^{\ell\top} \mathbf{U}^{\ell} \in \mathbb{R}^{\hat{r}^{\ell} \times r_1^{\ell}}, 
\hat{\mathbf{B}}^{\ell} := \mathbf{P}^{\ell\top} \mathbf{B}^{\ell} \in \mathbb{R}^{\hat{r}^{\ell} \times r_2^{\ell}}.$$

Thus, the reduced representation defines a smaller LRNR whose width is now given by  $\hat{r}^{\ell}$  and  $r_1^{\ell} + r_2^{\ell}$ . We call this compressed model **FastLRNR**, denoted by  $\hat{u}$ . It is expressed as

(6.9) 
$$\mathbf{z}^{\ell} = \sigma \left( \hat{\mathbf{U}}^{\ell} \operatorname{diag}(\mathbf{s}_{1}^{\ell}) \, \hat{\mathbf{V}}^{\ell \top} \mathbf{z}^{\ell-1} + \hat{\mathbf{B}}^{\ell} \mathbf{s}_{2}^{\ell} \right),$$
$$\mathbf{z}^{L} = \hat{\mathbf{U}}^{L} \operatorname{diag}(\mathbf{s}_{1}^{L}) \, \mathbf{z}^{L-1} + \mathbf{b}^{L}.$$

Recall that  $\mathbf{s}_1^{\ell}$ ,  $\mathbf{s}_2^{\ell}$  are truncated coefficients projected onto hypermodes via the reduced hypernetwork  $\hat{f}_{\text{hyper}}$ .

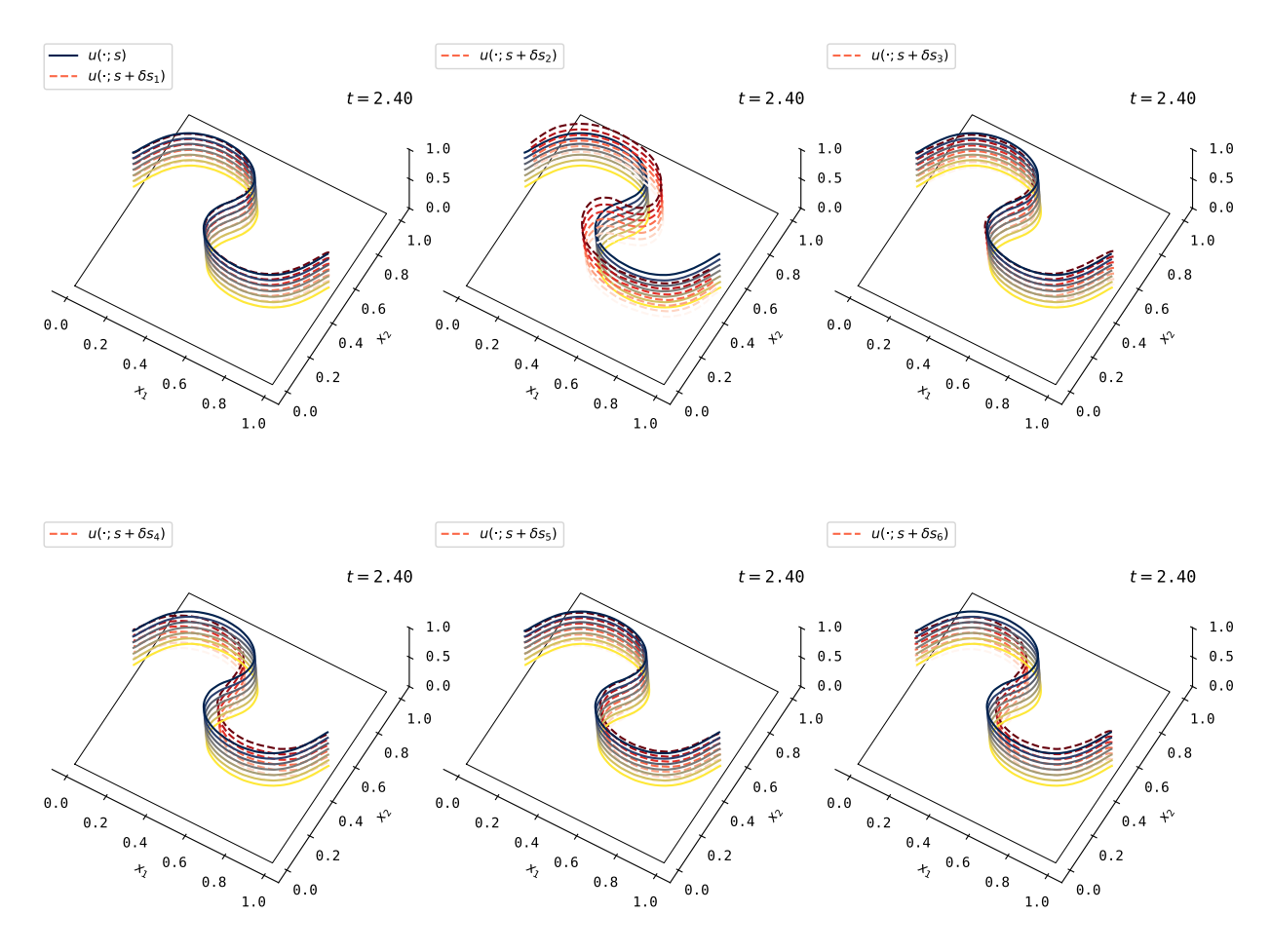


FIGURE 15. 2d advection equation example: LRNR reconstruction (solid contours) and the effect of coefficient perturbations along various hypermode directions (dashed contours) at a fixed time.

6.2. **Point evaluation.** We consider the application of FastLRNR construction above for pointwise evaluation. Specifically, we aim to evaluate the output of the network at a spatial point  $\mathbf{x}$  at various times t

(6.10) 
$$u(\mathbf{x}; \hat{f}_{hyper}(t)) \quad \text{for} \quad t \in [0, T].$$

To compute u, all intermediate hidden states  $\mathbf{z}^{\ell}$  must be evaluated layer by layer. The dominant computational cost arises from matrix-vector multiplications, particularly the multiplications by the weight matrices in each layer. This makes the overall evaluation complexity heavily dependent on the width and depth of the network.

Throughout this procedure, we fix a spatial point  $\mathbf{x}$  within the domain and estimate the basis  $\mathbf{\Xi}^{\ell}$  for each hidden state  $\mathbf{z}^{\ell}$  by sampling its values over different time instances t. Specifically, we form the snapshot matrix

(6.11) 
$$\left[\mathbf{z}^{\ell}(\mathbf{x}; f_{\text{hyper}}(t_1)) \mid \mathbf{z}^{\ell}(\mathbf{x}; f_{\text{hyper}}(t_2)) \mid \dots \mid \mathbf{z}^{\ell}(\mathbf{x}; f_{\text{hyper}}(t_N))\right],$$

and compute its singular value decomposition (SVD) to obtain the basis matrix  $\mathbf{\Xi}^{\ell}$ . Next, we apply the Empirical Interpolation Method (EIM) [3, 21] to determine the interpolation (or sampling) matrix  $\mathbf{P}^{\ell}$ . With these components in place, we construct the FastLRNR model, which we then use to efficiently approximate the evaluation (6.10).

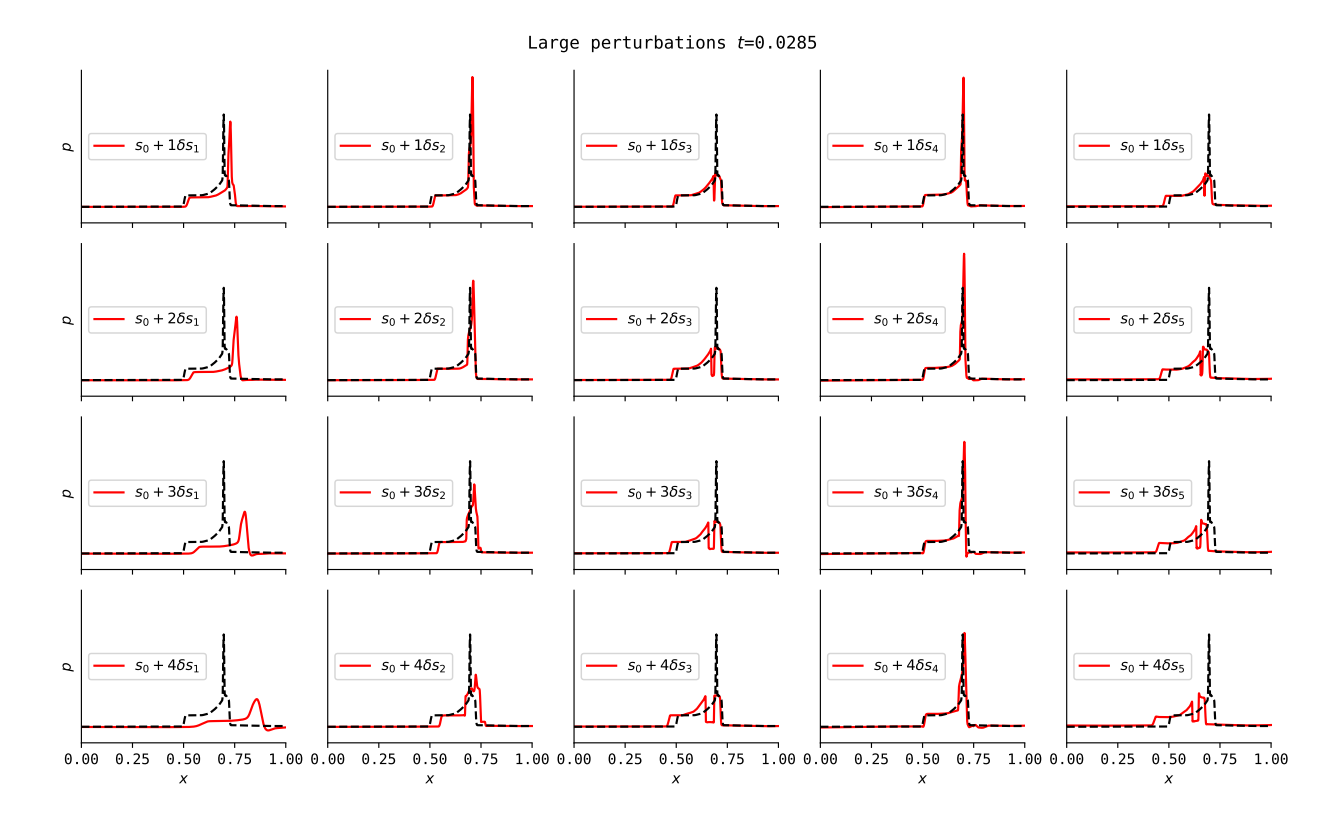


FIGURE 16. Coefficient extrapolation (large perturbations) along the hypermode directions for the 1d Euler example, starting from the reconstruction at time t = 0.0285. Each column shows the effect of perturbing along a dominant hypermode. The same hypermodes and base time were used in Fig. 9.

The results for our examples are shown in Fig. 17. The reconstructed solutions from FastLRNR agree well with those of the full model, despite FastLRNR using a significantly smaller architecture. As a result, it can be evaluated much more efficiently, with the number of floating-point operations scaling with the reduced width of the FastLRNR. According to recent work in the INR literature, such network sizes approach the regime required for real-time rendering applications [79, 57].

The FastLRNR construction relies on the fact that the hidden units  $\mathbf{z}^{\ell}$  above lie in a low-rank subspace, a property that is unique to LRNRs: Low-rankness in the hidden units is not observed in other techniques enforcing low-rankness in the weights [56, 54, 35], or in other hypernetwork approaches [48, 101, 83].

We remind the reader that FastLRNR can also be used to approximate backpropagation operations for solving partial differential equations [26], thereby enabling its integration with numerical solvers. This opens the door for FastLRNRs to be employed not only for efficient inference but also as components in physics-informed and hybrid computational frameworks.

### 7. SPATIAL EXTRAPOLATION IN PERIODIC BOUNDARY CONDITIONS

For linear low-dimensional representations, handling incoming boundary conditions, particularly where wave profiles enter the domain, remains a challenging problem, primarily due to the slow decay of the Kolmogorov *n*-width. However, in two of our examples, the meta-learning framework appears to emulate periodic boundary conditions without introducing visible artifacts. A plausible explanation for how LRNRs manage boundaries is as follows: the low-rank structure of LRNRs promotes an economical reconstruction of the solution, effectively prioritizing physically plausible

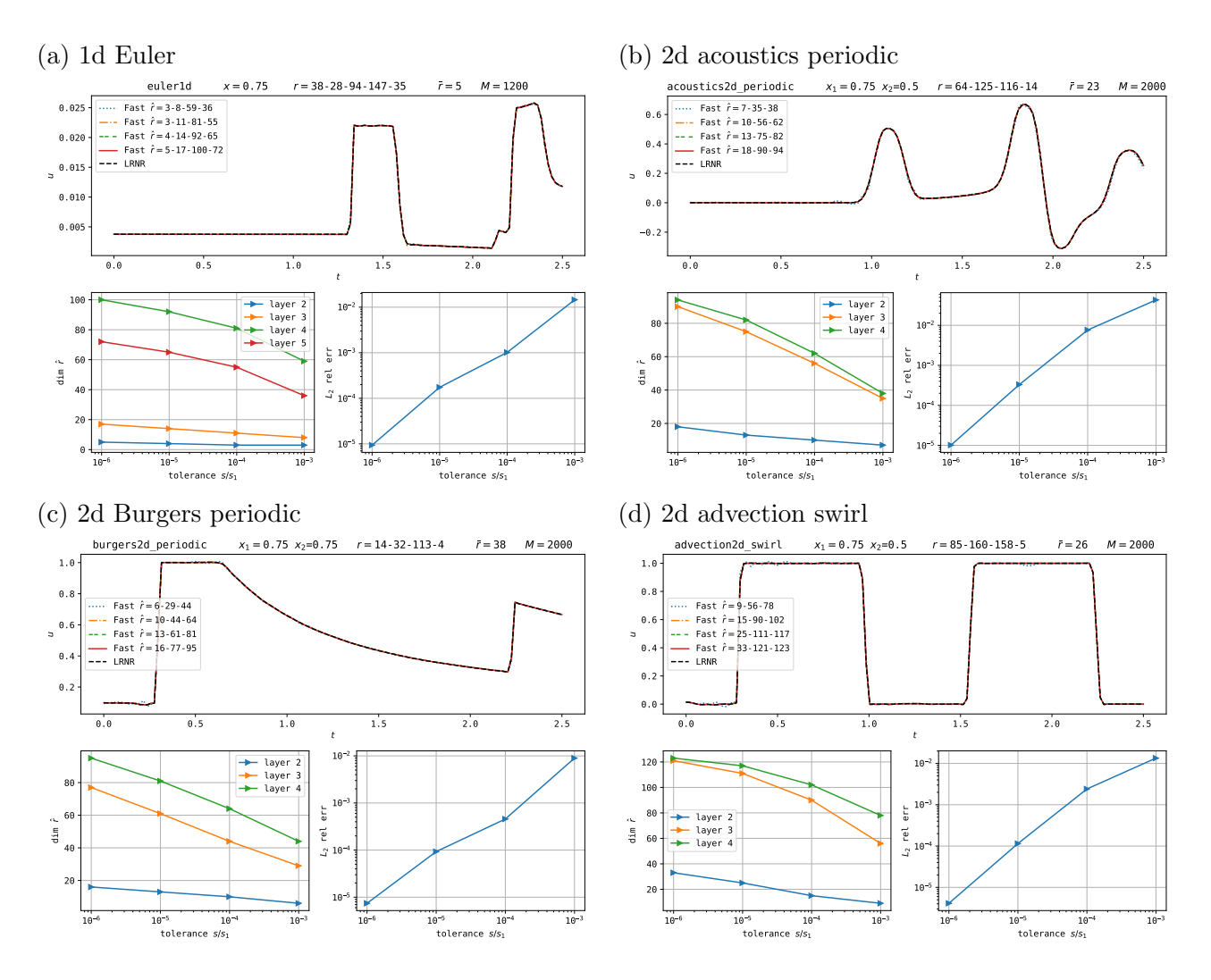


FIGURE 17. FastLRNR evaluation results for varying EIM ranks. As the EIM rank increases, the  $\ell_2$  relative error consistently decreases, reaching below  $10^{-4}$  when compared to full LRNR evaluation. The EIM rank  $\hat{r}^{\ell}$  remains comparable to the rank of the weight matrices  $r_1^{\ell}$  in the examples.

wave propagation. This behavior aligns with the nature of hyperbolic waves, where information is transported along characteristic curves. The resulting reconstruction approximately respects causality and maintains information flow within the domain of influence.

To investigate how the trained LRNRs approximate boundary values, we evaluate the LRNR over a spatially extended domain. Since the LRNR was not exposed to any data outside the original spatial domain during training, this evaluation amounts to spatial extrapolation. The results for the 2d Burgers and acoustics equations are shown in Fig. 18. Remarkably, the LRNR continues to exhibit coherent and physically plausible features even beyond the training domain.

7.1. **2d acoustics equation.** Focusing on the 2d acoustics equations (Fig. 18, top), we observe that at time t = 0.19, the compactly supported initial condition is extended beyond the spatial domain in a pseudo-periodic manner. While the extension is not exact, the extrapolated waveforms propagate in a fashion similar to the interior solution, which is accurately represented. As these extrapolated waves enter the domain, any initial inaccuracies are corrected near the boundary:

although the waveforms appear slightly distorted outside, they recover physically plausible shapes upon entry.

At time t=0.38, the outgoing waves continue to retain their structure for some distance, although distortion increases as they propagate further from the domain. By time t=0.64 (near the final time t=0.75), the LRNR no longer maintains coherent incoming waveforms outside the domain. For instance, the solution just beyond the lower boundary shows no discernible wave features. Similarly, the upper-left and upper-right corners display little recognizable structure. This behavior aligns with the hyperbolic wave perspective, where the LRNR appears to implicitly respect the domain of influence by maintaining accurate waveforms only to the extent that they impact the solution within the spatial domain.

7.2. **2d Burgers equation.** Similar observations hold for the 2d Burgers' equation. However, a key distinction from the acoustics case is that the solution here propagates strictly along characteristic curves. This difference is apparent already at the initial time t=0.62: in the upper-right corner outside the square domain, no physically meaningful profiles are present, and the extrapolated behavior resembles what is typically observed when INRs are queried outside their training domain. We hypothesize that this is due to the learned directionality of wave propagation. The trained LRNR appears to have implicitly learned the characteristics of the PDE and thus omits wave structures in regions that lie outside the domain of influence, i.e., regions from which no characteristics reach the interior of the domain.

In contrast, in other directions, the LRNR places extrapolated structures that resemble severely distorted periodic extensions of the solution inside the domain. At time t = 1.50, these distorted features propagate along the general direction of wave motion and gradually morph into accurate wave profiles as they enter the domain. Between these propagating structures, we observe regions containing irregularities or "wrinkles," which seem to be occluded once they are inside the domain.

Meanwhile, the outgoing shock retains its general form as it leaves the domain; however, its tip becomes smoothed, deviating from the physically expected sharp profile and rendering it unphysical. By t=2.50, the intruding wavefronts at the upper-left and lower-right parts of the domain have evolved into straight rarefaction slopes that continue outside the spatial domain. As the domain of influence contracts over time, the LRNR representation outside the domain exhibits increasingly random features, consistent with the loss of physical relevance in those regions.

Overall, the LRNR reconstruction appears to implicitly respect the finite propagation speed and the domain of influence characteristic of hyperbolic systems.

#### 8. Conclusion

This work introduced the Low-Rank Neural Representation (LRNR), a novel architecture that enables efficient, interpretable, and physically meaningful modeling of hyperbolic wave phenomena. By imposing a layer-wise low-rank structure and leveraging a hypernetwork to capture temporal dynamics, LRNRs achieve compact representations while preserving the rich behaviors of nonlinear wave interactions, including shocks and rarefactions. We demonstrated that these representations not only interpolate well but also extrapolate meaningfully along learned hypermodes, revealing dominant modes of variation even far from the training data. The compressed FastLRNR variant further enables rapid evaluation and backpropagation, making it practical for use in real-time and PDE-constrained settings. Additionally, we showed that LRNRs implicitly respect causality and handle domain boundaries through the learned propagation dynamics. These findings suggest that LRNRs provide a compelling architecture for scientific machine learning, particularly for systems where structure, interpretability, and computational efficiency are required.

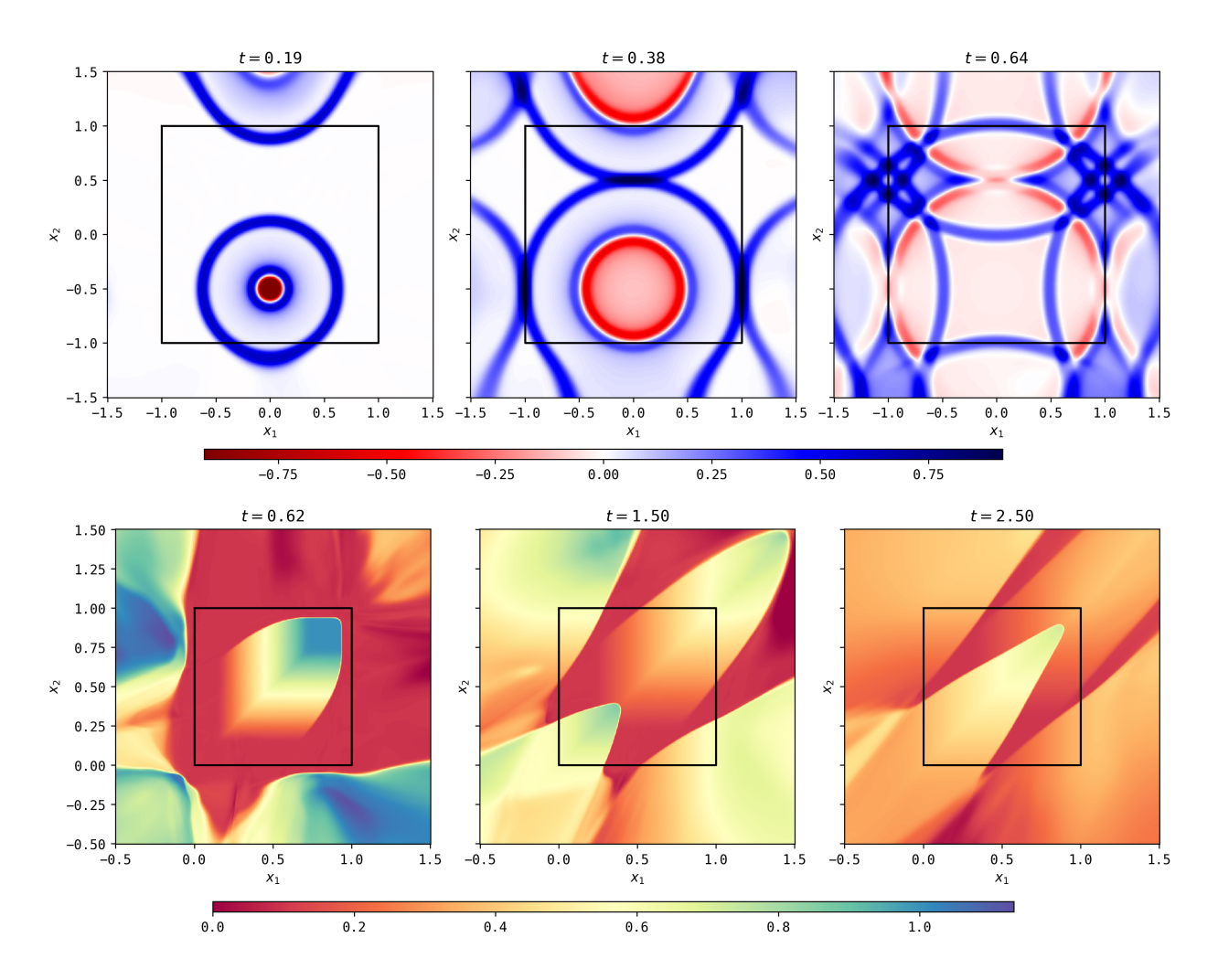


FIGURE 18. Evaluation of LRNR reconstruction of the 2d acoustics (top) and 2d Burgers (bottom) equations with periodic boundary conditions, evaluated outside the square domain on which the training data was provided.

# 9. Acknowledgements

The authors acknowledge the Research Infrastructure Services (RIS) group at Washington University in St. Louis for providing computational resources and services needed to generate the research results delivered within this paper (URL: https://ris.wustl.edu).

K. Lee acknowledges support from the U.S. National Science Foundation under grant IIS 2338909. N. Park was supported by Samsung Research Funding & Incubation Center of Samsung Electronics under Project Number SRFC-IT2402-08, and by Samsung Electronics Co., Ltd. (No. G01240136, KAIST Semiconductor Research Fund (2nd)). Part of this work was done while D. Rim was enjoying the hospitality of University of Washington in Seattle as a Visiting Scholar. He thanks R. J. LeVeque, Jesse Chan, Kui Ren, and Gunther Uhlmann for helpful discussions.

# APPENDIX A. PLANAR WAVE DECOMPOSITIONS

Consider the free space wave equation in d dimensions, which seeks  $u: \mathbb{R}^d \times \mathbb{R}_+ \to \mathbb{R}$  that satisfies

(A.1) 
$$\begin{cases} (\partial_{tt} - c^2 \Delta) u = 0 & \text{in } \mathbb{R}^d \times \mathbb{R}_+, \\ u(\cdot, 0) = u_0, \\ \partial_t u(\cdot, 0) = v_0. \end{cases}$$

We decompose the problem into two parts, one with zero initial velocity and the other zero initial value, which reads

(A.2) 
$$\begin{cases} (\partial_{tt} - c^2 \Delta) u = 0, \\ u(\cdot, 0) = u_0, \\ \partial_t u(\cdot, 0) = 0, \end{cases} \begin{cases} (\partial_{tt} - c^2 \Delta) u = 0, \\ u(\cdot, 0) = 0, \\ \partial_t u(\cdot, 0) = v_0, \end{cases}$$

then denote the solutions to the two problems by  $u^{(1)}$  and  $u^{(2)}$ , respectively, with  $u = u^{(1)} + u^{(2)}$ . Now, consider the planar initial conditions

(A.3) 
$$u_0(\mathbf{x}) = g(\mathbf{w} \cdot \mathbf{x}), \quad v_0(\mathbf{x}) = h(\tilde{\mathbf{w}} \cdot \mathbf{x}), \quad \mathbf{w}, \tilde{\mathbf{w}} \in S^{d-1}$$

for some 1d functions  $g, h : \mathbb{R} \to \mathbb{R}$ . Letting the solution ansatz be

(A.4) 
$$u^{(1)}(\mathbf{x},t) = G(\mathbf{w} \cdot \mathbf{x},t), \qquad u^{(2)}(\mathbf{x},t) = H(\tilde{\mathbf{w}} \cdot \mathbf{x},t),$$

one reduces the wave equation to their 1d analogues due to the intertwining relation (3.7),

(A.5) 
$$\begin{cases} (\partial_{tt} - c^2 \partial_{\beta\beta})G = 0, \\ G(\cdot, 0) = g, \\ \partial_t G(\cdot, 0) = 0, \end{cases} \begin{cases} (\partial_{tt} - c^2 \partial_{\beta\beta})H = 0, \\ H(\cdot, 0) = 0, \\ \partial_t H(\cdot, 0) = h. \end{cases}$$

The solution to these 1d problems are given by the d'Alembert solution (1.1),

(A.6) 
$$u^{(1)}(\mathbf{x},t) = \frac{1}{2} \left( g(\mathbf{w} \cdot \mathbf{x} + ct) + g(\mathbf{w} \cdot \mathbf{x} - ct) \right),$$
$$u^{(2)}(\mathbf{x},t) = \frac{1}{2c} \int_{\tilde{\mathbf{w}} \cdot \mathbf{x} - ct}^{\tilde{\mathbf{w}} \cdot \mathbf{x} + ct} h(\beta) \, \mathrm{d}\beta = \frac{1}{2c} \left( \tilde{h}(\tilde{\mathbf{w}} \cdot \mathbf{x} + ct) - \tilde{h}(\tilde{\mathbf{w}} \cdot \mathbf{x} - ct) \right),$$

where  $\tilde{h}(\beta) := \int_0^\beta h(\zeta) d\zeta$  denotes the antiderivative. Then, the solution to the original free space problem (A.1) is the sum  $u = u^{(1)} + u^{(2)}$ .

Superposition of planar waves. In the case the initial condition was given by the superposition

(A.7) 
$$u_0(\mathbf{x}) = \sum_{i=1}^{\infty} g_i(\mathbf{w}_i \cdot \mathbf{x}), \qquad v_0(\mathbf{x}) = \sum_{i=1}^{\infty} h_i(\tilde{\mathbf{w}}_i \cdot \mathbf{x}), \qquad \mathbf{w}_i, \tilde{\mathbf{w}}_i \in S^{d-1},$$

the solution is obtained by applying the solution (A.6) termwise,

(A.8) 
$$u(\mathbf{x},t) = \frac{1}{2} \sum_{i=1}^{\infty} \left( g_i(\mathbf{w}_i \cdot \mathbf{x} + ct) + g_i(\mathbf{w}_i \cdot \mathbf{x} - ct) \right) + \frac{1}{2c} \sum_{i=1}^{\infty} \left( \tilde{h}_i(\tilde{\mathbf{w}}_i \cdot \mathbf{x} + ct) - \tilde{h}_i(\tilde{\mathbf{w}}_i \cdot \mathbf{x} - ct) \right),$$

with  $\tilde{h}_i(\beta) := \int_0^\beta h_i(\zeta) d\zeta$ .

More generally, we can consider the planar waves that are continuously parametrized. That is, consider the functions g and h indexed by the real tuple (a, b), of the form

(A.9) 
$$g_{a,b}(\mathbf{w} \cdot \mathbf{x}) = a\sigma(\mathbf{w} \cdot \mathbf{x} + b), \qquad h_{a,b}(\mathbf{w} \cdot \mathbf{x}) = a\sigma'(\mathbf{w} \cdot \mathbf{x} + b),$$

where  $\sigma$  and  $\sigma'$  are the ReLU function and its derivative, respectively, and the initial conditions can be written as the integrals

(A.10) 
$$u_0(\mathbf{x}, t) = \int g_{a,b}(\mathbf{w} \cdot \mathbf{x}) \, d\mu(da, d\mathbf{w}, db) = \int a\sigma(\mathbf{w} \cdot \mathbf{x} + b) \, d\mu(da, d\mathbf{w}, db),$$
$$v_0(\mathbf{x}, t) = \int h_{a,b}(\mathbf{w} \cdot \mathbf{x}) \, d\nu(da, d\mathbf{w}, db) = \int a\sigma'(\mathbf{w} \cdot \mathbf{x} + b) \, d\nu(da, d\mathbf{w}, db),$$

for given probability measures  $\mu$  and  $\nu$  over  $\mathbb{R} \times S^{d-1} \times \mathbb{R}$ . The wave solution is then

(A.11) 
$$u(\mathbf{x},t) = \frac{1}{2} \int a \left[ \sigma(\mathbf{w} \cdot \mathbf{x} + b + ct) + \sigma(\mathbf{w} \cdot \mathbf{x} + b - ct) \right] d\mu(da, d\mathbf{w}, db) + \frac{1}{2c} \int a \left[ \sigma(\mathbf{w} \cdot \mathbf{x} + b + ct) - \sigma(\mathbf{w} \cdot \mathbf{x} + b - ct) \right] d\nu(da, d\mathbf{w}, db).$$

### References

- [1] R. ABGRALL, D. AMSALLEM, AND R. CRISOVAN, Robust model reduction by L<sup>1</sup>-norm minimization and approximation via dictionaries: Application to linear and nonlinear hyperbolic problems, Advanced Modeling and Simulation in Engineering Sciences, 3 (2016), p. 1.
- [2] E. L. Allgower and K. Georg, *Introduction to Numerical Continuation Methods*, Society for Industrial and Applied Mathematics, 2003.
- [3] M. BARRAULT, Y. MADAY, N. C. NGUYEN, AND A. T. PATERA, An 'empirical interpolation' method: application to efficient reduced-basis discretization of partial differential equations, Comptes Rendus Mathematique, 339 (2004), pp. 667 672.
- [4] R. Basri, M. Galun, A. Geifman, D. Jacobs, Y. Kasten, and S. Kritchman, Frequency bias in neural networks for input of non-uniform density, vol. 119 of Proceedings of Machine Learning Research, 2020, pp. 685– 694.
- [5] Y. Bengio, J. Louradour, R. Collobert, and J. Weston, *Curriculum learning*, in Proceedings of the 26th Annual International Conference on Machine Learning, 2009, pp. 41–48.
- [6] P. Benner, S. Gugercin, and K. Willcox, A Survey of Projection-Based Model Reduction Methods for Parametric Dynamical Systems, SIAM Review, 57 (2015), pp. 483-531.
- [7] M. J. Berger and R. J. Leveque, Adaptive Mesh Refinement Using Wave-Propagation Algorithms for Hyperbolic Systems, SIAM Journal on Numerical Analysis, 35 (1998), pp. 2298–2316.
- [8] M. J. Berger and J. Oliger, Adaptive mesh refinement for hyperbolic partial differential equations, Journal of Computational Physics, 53 (1984), pp. 484–512.
- [9] G. Berkooz, P. Holmes, and J. L. Lumley, The Proper Orthogonal Decomposition in the Analysis of Turbulent Flows, Annual Review of Fluid Mechanics, 25 (1993), pp. 539–575.
- [10] J. BERNER, P. GROHS, G. KUTYNIOK, AND P. PETERSEN, The Modern Mathematics of Deep Learning, Cambridge University Press, Cambridge, UK, 2022.
- [11] W. J. BEYN AND V. THÜMMLER, Freezing Solutions of Equivariant Evolution Equations, SIAM Journal on Applied Dynamical Systems, 3 (2004), pp. 85–116.
- [12] K. Bhattacharya, B. Hosseini, N. B. Kovachki, and A. M. Stuart, *Model Reduction And Neural Networks For Parametric PDEs*, The SMAI Journal of Computational Mathematics, 7 (2021), pp. 121–157.
- [13] B. BIGGIO, I. CORONA, D. MAIORCA, B. NELSON, N. ŠRNDIĆ, P. LASKOV, G. GIACINTO, AND F. ROLI, Evasion Attacks against Machine Learning at Test Time, in Machine Learning and Knowledge Discovery in Databases, H. Blockeel, K. Kersting, S. Nijssen, and F. Železný, eds., Springer Berlin Heidelberg, 2013, pp. 387– 402.
- [14] H. BÖLCSKEI, P. GROHS, G. KUTYNIOK, AND P. PETERSEN, Optimal Approximation with Sparsely Connected Deep Neural Networks, SIAM Journal on Mathematics of Data Science, 1 (2019), pp. 8-45.
- [15] N. BONNEEL, J. RABIN, G. PEYRÉ, AND H. PFISTER, Sliced and Radon Wasserstein barycenters of measures, Journal of Mathematical Imaging and Vision, 51 (2015), pp. 22–45.
- [16] C. BUCILUĂ, R. CARUANA, AND A. NICULESCU-MIZIL, Model compression, in Proceedings of the 12th ACM SIGKDD International Conference on Knowledge Discovery and Data Mining, New York, NY, USA, 2006, pp. 535–541.
- [17] N. CAGNIART, Y. MADAY, AND B. STAMM, Model Order Reduction for Problems with Large Convection Effects, Springer International Publishing, Cham, Switzerland, 2019, pp. 131–150.
- [18] E. CANDÈS, L. DEMANET, AND L. YING, Fast Computation of Fourier Integral Operators, SIAM Journal on Scientific Computing, 29 (2007), pp. 2464–2493.

- [19] E. CANDÈS, L. DEMANET, AND L. YING, A Fast Butterfly Algorithm for the Computation of Fourier Integral Operators, Multiscale Modeling & Simulation, 7 (2009), pp. 1727–1750.
- [20] E. J. CANDÈS AND L. DEMANET, The curvelet representation of wave propagators is optimally sparse, Communications on Pure and Applied Mathematics, 58 (2005), pp. 1472–1528.
- [21] S. CHATURANTABUT AND D. C. SORENSEN, Nonlinear Model Reduction via Discrete Empirical Interpolation, SIAM Journal on Scientific Computing, 32 (2010), pp. 2737–2764.
- [22] Y. CHEN, Y. JI, A. NARAYAN, AND Z. XU, TGPT-PINN: Nonlinear model reduction with transformed GPT-PINNs, Computer Methods in Applied Mechanics and Engineering, 430 (2024), p. 117198.
- [23] Z. CHEN, V. BADRINARAYANAN, C.-Y. LEE, AND A. RABINOVICH, GradNorm: Gradient Normalization for Adaptive Loss Balancing in Deep Multitask Networks, in Proceedings of the 35th International Conference on Machine Learning, J. Dy and A. Krause, eds., vol. 80 of Proceedings of Machine Learning Research, 2018, pp. 794–803.
- [24] Y. CHENG, D. WANG, P. ZHOU, AND T. ZHANG, A survey of model compression and acceleration for deep neural networks, (2017), arXiv:1710.09282.
- [25] Y. CHENG, D. WANG, P. ZHOU, AND T. ZHANG, Model Compression and Acceleration for Deep Neural Networks: The Principles, Progress, and Challenges, IEEE Signal Processing Magazine, 35 (2018), pp. 126–136.
- [26] W. CHO, K. LEE, N. PARK, D. RIM, AND G. WELPER, FastLRNR and Sparse Physics Informed Backpropagation, Results in Applied Mathematics, 25 (2025), p. 100547.
- [27] W. Cho, K. Lee, D. Rim, and N. Park, Hypernetwork-based Meta-Learning for Low-Rank Physics-Informed Neural Networks, in Advances in Neural Information Processing Systems, vol. 36, Red Hook, NY, 2023, Curran Associates, Inc., pp. 11219–11231.
- [28] CLAWPACK DEVELOPMENT TEAM, Clawpack software, 2024, doi:10.5281/zenodo.13376470, http://www.clawpack.org. Version 5.11.0.
- [29] P. G. CONSTANTINE AND G. IACCARINO, Reduced order models for parameterized hyperbolic conservation laws with shock reconstruction, Center for Turbulence Research Annual Research Briefs, (2012).
- [30] M. CUTURI AND A. DOUCET, Fast Computation of Wasserstein Barycenters, in Proceedings of the 31st International Conference on Machine Learning, vol. 32 of Proceedings of Machine Learning Research, 2014, pp. 685–693.
- [31] C. M. Dafermos, Hyperbolic Conservation Laws in Continuum Physics, Springer Berlin Heidelberg, Berlin, Heidelberg, 2010.
- [32] W. Dahmen, Compositional Sparsity, Approximation Classes, and Parametric Transport Equations, (2023), arXiv:2207.06128.
- [33] W. Dahmen, G. Kutyniok, W.-Q. Lim, C. Schwab, and G. Welper, Adaptive anisotropic Petrov-Galerkin methods for first order transport equations, Journal of Computational and Applied Mathematics, 340 (2018), pp. 191–220.
- [34] J. DARBON AND T. MENG, On some neural network architectures that can represent viscosity solutions of certain high dimensional Hamilton-Jacobi partial differential equations, Journal of Computational Physics, 425 (2021), p. 109907.
- [35] DEEPSEEK-AI, D. GUO, D. YANG, H. ZHANG, J. SONG, R. ZHANG, R. XU, Q. ZHU, S. MA, P. WANG, X. BI, X. ZHANG, X. YU, Y. WU, Z. F. WU, Z. GOU, Z. SHAO, Z. LI, Z. GAO, A. LIU, B. XUE, B. WANG, B. Wu, B. Feng, C. Lu, C. Zhao, C. Deng, C. Zhang, C. Ruan, D. Dai, D. Chen, D. Ji, E. Li, F. Lin, F. Dai, F. Luo, G. Hao, G. Chen, G. Li, H. Zhang, H. Bao, H. Xu, H. Wang, H. Ding, H. Xin, H. Gao, H. Qu, H. Li, J. Guo, J. Li, J. Wang, J. Chen, J. Yuan, J. Qiu, J. Li, J. L. Cai, J. NI, J. LIANG, J. CHEN, K. DONG, K. HU, K. GAO, K. GUAN, K. HUANG, K. YU, L. WANG, L. ZHANG, L. Zhao, L. Wang, L. Zhang, L. Xu, L. Xia, M. Zhang, M. Zhang, M. Tang, M. Li, M. Wang, M. Li, N. Tian, P. Huang, P. Zhang, Q. Wang, Q. Chen, Q. Du, R. Ge, R. Zhang, R. Pan, R. Wang, R. J. Chen, R. L. Jin, R. Chen, S. Lu, S. Zhou, S. Chen, S. Ye, S. Wang, S. Yu, S. Zhou, S. Pan, S. S. LI, S. ZHOU, S. WU, S. YE, T. YUN, T. PEI, T. SUN, T. WANG, W. ZENG, W. ZHAO, W. LIU, W. LIANG, W. Gao, W. Yu, W. Zhang, W. L. Xiao, W. An, X. Liu, X. Wang, X. Chen, X. Nie, X. Cheng, X. Liu, X. XIE, X. LIU, X. YANG, X. LI, X. SU, X. LIN, X. Q. LI, X. JIN, X. SHEN, X. CHEN, X. SUN, X. WANG, X. Song, X. Zhou, X. Wang, X. Shan, Y. K. Li, Y. Q. Wang, Y. X. Wei, Y. Zhang, Y. Xu, Y. Li, Y. Zhao, Y. Sun, Y. Wang, Y. Yu, Y. Zhang, Y. Shi, Y. Xiong, Y. He, Y. Piao, Y. Wang, Y. Tan, Y. MA, Y. LIU, Y. GUO, Y. OU, Y. WANG, Y. GONG, Y. ZOU, Y. HE, Y. XIONG, Y. LUO, Y. YOU, Y. LIU, Y. ZHOU, Y. X. ZHU, Y. XU, Y. HUANG, Y. LI, Y. ZHENG, Y. ZHU, Y. MA, Y. TANG, Y. ZHA, Y. YAN, Z. Z. Ren, Z. Ren, Z. Sha, Z. Fu, Z. Xu, Z. Xie, Z. Zhang, Z. Hao, Z. Ma, Z. Yan, Z. Wu, Z. Gu, Z. Zhu, Z. Liu, Z. Li, Z. Xie, Z. Song, Z. Pan, Z. Huang, Z. Xu, Z. Zhang, and Z. Zhang, DeepSeek-R1: Incentivizing Reasoning Capability in LLMs via Reinforcement Learning, (2025), arXiv:2501.12948.
- [36] R. DEVORE, B. HANIN, AND G. PETROVA, Neural network approximation, Acta Numerica, 30 (2021), pp. 327–444.

- [37] R. A. DEVORE, Nonlinear approximation, Acta Numerica, 7 (1998), pp. 51–150.
- [38] W. E, C. MA, AND L. Wu, The Barron Space and the Flow-Induced Function Spaces for Neural Network Models, Constructive Approximation, 55 (2022), pp. 369-406.
- [39] V. EHRLACHER, D. LOMBARDI, O. MULA, AND F.-X. VIALARD, Nonlinear model reduction on metric spaces. Application to one-dimensional conservative PDEs in Wasserstein spaces, ESAIM: Mathematical Modelling and Numerical Analysis, 54 (2020), pp. 2159–2197.
- [40] L. C. Evans, Partial differential equations, American Mathematical Society, Providence, RI, USA, 2nd ed., 2010.
- [41] G. B. FOLLAND, Introduction to Partial Differential Equations, Princeton University Press, 2nd ed., 1995.
- [42] W. D. FRIES, X. HE, AND Y. CHOI, LaSDI: Parametric Latent Space Dynamics Identification, Computer Methods in Applied Mechanics and Engineering, 399 (2022), p. 115436.
- [43] R. GEELEN, S. WRIGHT, AND K. WILLCOX, Operator inference for non-intrusive model reduction with quadratic manifolds, Computer Methods in Applied Mechanics and Engineering, 403 (2023), p. 115717.
- [44] M. Geist, P. Petersen, M. Raslan, R. Schneider, and G. Kutyniok, *Numerical Solution of the Parametric Diffusion Equation by Deep Neural Networks*, Journal of Scientific Computing, 88 (2021), p. 22.
- [45] J.-F. Gerbeau and D. Lombardi, Approximated Lax pairs for the reduced order integration of nonlinear evolution equations, Journal of Computational Physics, 265 (2014), pp. 246 269.
- [46] J.-L. GUERMOND, F. MARPEAU, AND B. POPOV, A fast algorithm for solving first-order PDEs by L<sup>1</sup>-minimization, Communications in Mathematical Sciences, 6 (2008), pp. 199 216.
- [47] J.-L. GUERMOND AND B. POPOV, Linear Advection with Ill-Posed Boundary Conditions via L<sup>1</sup>-Minimization, International Journal of Numerical Analysis and Modeling, 4 (2007), pp. 39–47.
- [48] D. HA, A. DAI, AND Q. V. LE, Hypernetworks, (2016), arXiv:1609.09106.
- [49] J. HESTHAVEN AND S. UBBIALI, Non-intrusive reduced order modeling of nonlinear problems using neural networks, Journal of Computational Physics, 363 (2018), pp. 55–78.
- [50] J. S. Hesthaven, G. Rozza, and B. Stamm, Certified Reduced Basis Methods for Parametrized Partial Differential Equations, Springer, Cham, 2016.
- [51] J. S. HESTHAVEN AND T. WARBURTON, Nodal Discontinuous Galerkin Methods, vol. 54 of Texts in Applied Mathematics, Springer, New York, 2008. Algorithms, analysis, and applications.
- [52] A. A. HEYDARI, C. A. THOMPSON, AND A. MEHMOOD, SoftAdapt: Techniques for Adaptive Loss Weighting of Neural Networks with Multi-Part Loss Functions, (2019), arXiv:1912.12355.
- [53] G. HINTON, O. VINYALS, AND J. DEAN, Distilling the Knowledge in a Neural Network, (2015), arXiv:1503.02531.
- [54] E. J. Hu, Y. Shen, P. Wallis, Z. Allen-Zhu, Y. Li, S. Wang, L. Wang, and W. Chen, LoRA: Low-Rank Adaptation of Large Language Models, in International Conference on Learning Representations, 2022.
- [55] A. IOLLO AND D. LOMBARDI, Advection modes by optimal mass transfer, Physical Review E, 89 (2014), p. 022923.
- [56] M. Jaderberg, A. Vedaldi, and A. Zisserman, Speeding up Convolutional Neural Networks with Low Rank Expansions, (2014), arXiv:1405.3866.
- [57] B. KERBL, G. KOPANAS, T. LEIMKUEHLER, AND G. DRETTAKIS, 3D Gaussian Splatting for Real-Time Radiance Field Rendering, ACM Transactions on Graphics, 42 (4) (2023).
- [58] D. P. Kingma and J. Ba, Adam: A Method for Stochastic Optimization, International Conference for Learning Representations, (2015).
- [59] O. KOCH AND C. LUBICH, Dynamical Low-Rank Approximation, SIAM Journal on Matrix Analysis and Applications, 29 (2007), pp. 434–454.
- [60] P. KRAH, S. BÜCHHOLZ, M. HÄRINGER, AND J. REISS, Front Transport Reduction for Complex Moving Fronts, Journal of Scientific Computing, 96 (2023), p. 28.
- [61] G. Kutyniok and D. Labate, Shearlets: Multiscale Analysis for Multivariate Data, Birkhäuser Boston, Boston, 2012.
- [62] G. KUTYNIOK, P. PETERSEN, M. RASLAN, AND R. SCHNEIDER, A Theoretical Analysis of Deep Neural Networks and Parametric PDEs, Constructive Approximation, 55 (2022), pp. 73–125.
- [63] J. N. Kutz, S. L. Brunton, B. W. Brunton, and J. L. Proctor, Dynamic Mode Decomposition: Data-Driven Modeling of Complex Systems, Society for Industrial and Applied Mathematics, Philadelphia, PA, USA, 2016.
- [64] F. LAAKMANN AND P. PETERSEN, Efficient approximation of solutions of parametric linear transport equations by ReLU DNNs, Advances in Computational Mathematics, 47 (2021), p. 11.
- [65] P. D. LAX AND R. S. PHILLIPS, Scattering theory, Bull. Amer. Math. Soc., 70 (1964), pp. 130–142.
- [66] K. LEE AND K. T. CARLBERG, Model reduction of dynamical systems on nonlinear manifolds using deep convolutional autoencoders, Journal of Computational Physics, 404 (2020), p. 108973.

- [67] R. J. LEVEQUE, Finite Volume Methods for Hyperbolic Problems, Cambridge Texts in Applied Mathematics, Cambridge University Press, Cambridge, UK, 2002.
- [68] R. J. LEVEQUE, Finite Difference Methods for Ordinary and Partial Differential Equations, Society for Industrial and Applied Mathematics, 2007.
- [69] R. J. LEVEQUE, D. L. GEORGE, AND M. J. BERGER, Tsunami modelling with adaptively refined finite volume methods, Acta Numerica, 20 (2011), pp. 211–289.
- [70] R. LIAW, E. LIANG, R. NISHIHARA, P. MORITZ, J. E. GONZALEZ, AND I. STOICA, Tune: A Research Platform for Distributed Model Selection and Training, (2018), arXiv:1807.05118.
- [71] H. W. LIEPMANN AND A. ROSHKO, Elements of gasdynamics, John Wiley & Sons, 1957.
- [72] T. LONG, R. BARNETT, R. JEFFERSON-LOVEDAY, G. STABILE, AND M. ICARDI, A reduced-order model for advection-dominated problems based on the Radon Cumulative Distribution Transform, Advances in Computational Mathematics, 51 (2025), p. 5.
- [73] L. Lu, P. Jin, G. Pang, Z. Zhang, and G. E. Karniadakis, Learning nonlinear operators via DeepONet based on the universal approximation theorem of operators, Nature Machine Intelligence, 3 (2021), pp. 218–229.
- [74] R. MAJUMDAR, V. S. JADHAV, A. DEODHAR, S. KARANDE, L. VIG, AND V. RUNKANA, PIHLoRA: Physics-informed hypernetworks for low-ranked adaptation, in AI for Accelerated Materials Design NeurIPS 2023 Workshop, 2023.
- [75] Y. MAKOVOZ, Random Approximants and Neural Networks, Journal of Approximation Theory, 85 (1996), pp. 98–109.
- [76] S. MALLAT, A Wavelet Tour of Signal Processing (Third Edition), Academic Press, Boston, third edition ed., 2009.
- [77] C. MARCATI, J. A. A. OPSCHOOR, P. C. PETERSEN, AND C. SCHWAB, Exponential ReLU Neural Network Approximation Rates for Point and Edge Singularities, Foundations of Computational Mathematics, 23 (2022), pp. 1043–1127.
- [78] R. Mojgani and M. Balajewicz, Lagrangian basis method for dimensionality reduction of convection dominated nonlinear flows, (2017), arXiv:1701.04343.
- [79] T. MÜLLER, A. EVANS, C. SCHIED, AND A. KELLER, Instant neural graphics primitives with a multiresolution hash encoding, ACM Transactions on Graphics, 41 (4) (2022).
- [80] F. NATTERER, The Mathematics of Computerized Tomography, Society for Industrial and Applied Mathematics, Philadelphia, PA, 2001.
- [81] M. Ohlberger and S. Rave, Nonlinear reduced basis approximation of parameterized evolution equations via the method of freezing, Comptes Rendus Mathematique, 351 (2013), pp. 901 – 906.
- [82] M. Ohlberger and S. Rave, Reduced basis methods: Success, limitations and future challenges, Proceedings of the Conference Algoritmy, (2016), pp. 1–12.
- [83] S. Pan, S. L. Brunton, and J. N. Kutz, Neural Implicit Flow: a mesh-agnostic dimensionality reduction paradigm of spatio-temporal data, Journal of Machine Learning Research, 24 (2023), pp. 1–60.
- [84] J. J. Park, P. Florence, J. Straub, R. Newcombe, and S. Lovegrove, *DeepSDF: Learning Continuous Signed Distance Functions for Shape Representation*, in Proceedings of the IEEE/CVF Conference on Computer Vision and Pattern Recognition (CVPR), June 2019.
- [85] P. Petersen and F. Voigtlaender, Optimal approximation of piecewise smooth functions using deep ReLU neural networks, Neural Networks, 108 (2018), pp. 296–330.
- [86] A. Pinkus, n-Widths in Approximation Theory, Springer, Berlin, Heidelberg, 1985.
- [87] G. PISIER, Remarques sur un résultat non publié de B. Maurey, Séminaire d'analyse fonctionnelle, (1980-1981), pp. 1–12. talk:5.
- [88] N. RAHAMAN, A. BARATIN, D. ARPIT, F. DRAXLER, M. LIN, F. HAMPRECHT, Y. BENGIO, AND A. COURVILLE, On the Spectral Bias of Neural Networks, in Proceedings of the 36th International Conference on Machine Learning, K. Chaudhuri and R. Salakhutdinov, eds., vol. 97 of Proceedings of Machine Learning Research, 2019, pp. 5301–5310.
- [89] J. REISS, P. SCHULZE, J. SESTERHENN, AND V. MEHRMANN, The Shifted Proper Orthogonal Decomposition: A Mode Decomposition for Multiple Transport Phenomena, SIAM Journal on Scientific Computing, 40 (2018), pp. A1322–A1344.
- [90] D. RIM, Dimensional Splitting of Hyperbolic Partial Differential Equations Using the Radon Transform, SIAM Journal on Scientific Computing, 40 (2018), pp. A4184–A4207.
- [91] D. RIM AND K. MANDLI, Displacement Interpolation Using Monotone Rearrangement, SIAM/ASA Journal on Uncertainty Quantification, 6 (2018), pp. 1503-1531.
- [92] D. RIM, S. MOE, AND R. LEVEQUE, Transport Reversal for Model Reduction of Hyperbolic Partial Differential Equations, SIAM/ASA Journal on Uncertainty Quantification, 6 (2018), pp. 118–150.

- [93] D. RIM, B. PEHERSTORFER, AND K. T. MANDLI, Manifold Approximations via Transported Subspaces: Model Reduction for Transport-Dominated Problems, SIAM Journal on Scientific Computing, 45 (2023), pp. A170– A199
- [94] D. Rim, S. Suri, S. Hong, K. Lee, and R. J. Leveque, A Stability Analysis of Neural Networks and Its Application to Tsunami Early Warning, Journal of Geophysical Research: Machine Learning and Computation, 1 (2024), p. e2024JH000223.
- [95] D. RIM AND G. WELPER, Performance bounds for Reduced Order Models with Application to Parametric Transport, (2023), arXiv:2310.14391.
- [96] D. RIM AND G. WELPER, A Low Rank Neural Representation of Entropy Solutions, (2024), arXiv:2406.05694.
- [97] C. W. ROWLEY AND J. E. MARSDEN, Reconstruction equations and the Karhunen-Loève expansion for systems with symmetry, Physica D, 142 (2000), pp. 1–19.
- [98] T. P. SAPSIS AND P. F. LERMUSIAUX, Dynamically orthogonal field equations for continuous stochastic dynamical systems, Physica D: Nonlinear Phenomena, 238 (2009), pp. 2347–2360.
- [99] D. Serre, Systems of Conservation Laws 1: Hyperbolicity, Entropies, Shock Waves, Cambridge University Press, Cambridge, UK, 1999.
- [100] J. W. Siegel and J. Xu, Sharp Bounds on the Approximation Rates, Metric Entropy, and n-Widths of Shallow Neural Networks, Foundations of Computational Mathematics, 24 (2024), pp. 481–537.
- [101] V. SITZMANN, J. MARTEL, A. BERGMAN, D. LINDELL, AND G. WETZSTEIN, Implicit Neural Representations with Periodic Activation Functions, in Advances in Neural Information Processing Systems, vol. 33, Red Hook, NY, USA, 2020, Curran Associates, Inc., pp. 7462–7473.
- [102] C. SZEGEDY, W. ZAREMBA, I. SUTSKEVER, J. BRUNA, D. ERHAN, I. J. GOODFELLOW, AND R. FERGUS, Intriguing properties of neural networks, CoRR, abs/1312.6199 (2014).
- [103] T. TADDEI, A Registration Method for Model Order Reduction: Data Compression and Geometry Reduction, SIAM Journal on Scientific Computing, 42 (2020), pp. A997–A1027.
- [104] M. Van Dyke, An Album of Fluid Motion, Parabolic Press, 1982.
- [105] S. WANG, Y. TENG, AND P. PERDIKARIS, Understanding and Mitigating Gradient Flow Pathologies in Physics-Informed Neural Networks, SIAM Journal on Scientific Computing, 43 (2021), pp. A3055–A3081.
- [106] S. WANG, X. YU, AND P. PERDIKARIS, When and why PINNs fail to train: A neural tangent kernel perspective, Journal of Computational Physics, 449 (2022), p. 110768.
- [107] G. Welper, Interpolation of Functions with Parameter Dependent Jumps by Transformed Snapshots, SIAM Journal on Scientific Computing, 39 (2017), pp. A1225—A1250.
- [108] G. B. WHITHAM, Linear and nonlinear waves, Pure and applied mathematics, John Wiley & Sons, 1974.
- [109] M. V. WICKERHAUSER, Adapted Wavelet Analysis: From Theory to Software, AK Peters/CRC Press, 1996.
- [110] P. WOODWARD AND P. COLELLA, The numerical simulation of two-dimensional fluid flow with strong shocks, Journal of Computational Physics, 54 (1984), pp. 115–173.
- [111] P. R. WOODWARD, Trade-Offs in Designing Explicit Hydrodynamical Schemes for Vector Computers, in Parallel Computations, G. Rodrigue, ed., Academic Press, 1982, pp. 153–171.
- [112] H. Xu, H. Zhang, Z. Hu, X. Liang, R. Salakhutdinov, and E. Xing, AutoLoss: Learning Discrete Schedule for Alternate Optimization, in International Conference on Learning Representations, 2019.
- [113] Z.-Q. J. Xu, Y. Zhang, T. Luo, Y. Xiao, and Z. Ma, Frequency Principle: Fourier Analysis Sheds Light on Deep Neural Networks, Communications in Computational Physics, 28 (2020), pp. 1746–1767.
- [114] D. Yarotsky, Error bounds for approximations with deep ReLU networks, Neural Networks, 94 (2017), pp. 103–114.